Exploring the performance of 3D-printed custom piston-cylinder systems

by

E. Zillen

Faculty of Mechanical, Maritime
and Materials Engineering

TU Delft

Exploring the performance of 3D-printed custom piston-cylinder systems

by

E. Zillen

to obtain the degree of Master of Science
at the Delft University of Technology,
to be defended publicly on Thursday July 22, 2021 at 15:15 PM.

Course code:	ME51035	
Student number:	4215338	
Project duration:	November, 2020 – July, 2021	
Thesis committee:	Prof. Dr. Ing. H. Vallery,	TU Delft, committee chair, supervisor
	Dr. ir. G. Smit,	TU Delft, supervisor
	Dr. ir. M. J. Mirzaali,	TU Delft

An electronic version of this thesis is available at `http://repository.tudelft.nl/`.

TU Delft

PREFACE

Before you lies the result of my master thesis, the final project of my life as a student at the TU Delft. My journey in Delft began at the faculty of Industrial Design Engineering, where I got my bachelor's degree. After a challenging bridging program I ended up at the faculty of Mechanical, Maritime and Materials Engineering for my master's program in Mechanical Engineering. The final part of my program proved to be an interesting experience – graduating during the global Covid-19 pandemic.

This research would not have been possible without the help of numerous people. First of all, I would like to thank my outstanding supervisors, Heike Vallery and Gerwin Smit for the countless hours of feedback and the discussions in all the meetings during my project. Your enthusiasm and questions challenged me to always come up with even better solutions. Secondly, I would like to thank all the technical support I got during this project. A special thanks goes to Jan van Frankenhuyzen, for his valuable insights on designing and producing pneumatic components. To Damian de Nijs, Reinier van Antwerpen and Spiridon van Veldhove, thank you for your help producing the test models. And thanks to Jos van Driel, for his technical support on creating the test rig. Lastly I would like to thank the last member of my thesis committee, Mohammad Mirzaali, for taking the time to attend my presentation and review this work.

Most of all, I am gratefull for my wonderfull family and friends, without whom it would not have been possible to finish this thesis. A special gratitude to my partner Tim Booij, who supported me through all the ups and downs during this period – always encouraging me to keep going.

Eva Zillen
Delft, July 2021

LIST OF FIGURES

List of Tables

CONTENTS

Exploring the performance of 3D-printed custom piston-cylinder systems

Eva Zillen, Gerwin Smit, and Heike Vallery

ABSTRACT

Background Pneumatic actuators are widely used in applications like (medical) robots, or prosthetics. They require tight tolerances to keep them leakage-free. Over the last decade 3D-printing, or additive manufacturing, has emerged as a cost-effective production method in these applications. **Objective** The goal of this research is to study the possibility of creating a pneumatic linear actuator with additive manufacturing. The focus is on finding sealing mechanisms which can have a positive influence on preventing leakage and friction force in the 3D-printed actuator. Furthermore we aimed to use the advantage of 3D-printing to create pneumatic actuators with a non-circular cross-section. **Methodology** To evaluate the performance of a 3D-printed pneumatic actuator, a test setup is designed to measure the leakage and sliding friction force. Furthermore, we designed two pneumatic actuators with a non-conventional cross-sectional shape and validated their performance. **Results** The choice for the optimal sealing mechanism in 3D-printed pneumatic actuators depends on the application in mind. For low-pressure situations the single-acting cup-shaped NAPN sealing is recommended, with a measured friction force of $6.7\,\mathrm{N}$ at a pressure of $0.1\,\mathrm{MPa}$ for one entire movement cycle (extending and retracting stroke together). For high pressure situations the double acting KDN sealing shows the lowest friction force while remaining leakage-free ($13.5\,\mathrm{N}$ for the entire stroke at a pressure of $0.7\,\mathrm{MPa}$). Furthermore, we have proven it possible to print pneumatic cylinders with a non-cylindrical cross section. **Conclusion** We demonstrated a method to create leakage-free pneumatic linear actuators with additive manufacturing. For low pressure applications we showed first steps towards 3D-printed pneumatic actuators with non-circular cross-section of the piston, allowing more design freedom for these actuators.

KEYWORDS 3D-printing, additive manufacturing, pneumatic actuators, piston-cylinder systems

NOMENCLATURE

Abbreviation	Definition
ABS	Acrylonitril-Butarieen-Styreen
AM	Additive manufacturing
FDM	Fused deposition modeling
PLA	Polylactic acid
SLA	Stereolithography apparatus
SLM	Selective laser melting

All authors are with the Technical University of Delft e.zillen@student.tudelft.nl

I. INTRODUCTION

A. Additive manufacturing

The use of additive manufacturing (AM), also known as 3D printing or rapid prototyping, has become increasingly popular over the last decade [1]. With AM, three-dimensional objects are created in a layer-by-layer process where material is deposited, joined or solidified. The first published contribution of a solid three-dimensional model was made in 1981 by Hideo Kadoma — since then the technology has developed significantly [2]. As a result of this layer-by-layer production, AM comes with various benefits. The first, and for many people most important, benefit of AM is its high design freedom. Products with a high form complexity can be designed and created, such as internal passageways, or other features which are practically impossible to manufacture with conventional techniques [3]. The second advantage of AM is closely coupled to the high form freedom — the ability to create a personalised product. The third advantage of AM is the low production costs, as specialised and expensive manufacturing equipment is not necessary to create a product and can therefore even be used by hobbyists. This makes the technique ideal for rapid prototyping purposes. For these reasons the technology is actively being used in various industries, for example sporting goods, jewellery or fashion items, but also in more technical areas such as the robotics, automotive, and aerospace industries [4]. Besides the more commercial industries, the use of AM in the medical sector is also rapidly growing. AM is used to create medical tools, an overview of which can be found in the study of Culmone et al. [5], medical implants or devices like exoskeletons, prostheses, and orthoses [6]. The first 3D printing technique to be commercialised was stereolithography apparatus (SLA) [2]. SLA printing, also called resin printing, uses a photochemical process to form and solidify the layers. Light causes chemical monomers to form polymers in the form of the desired three-dimensional shape. An ultraviolet laser is focused on a reservoir of liquid photopolymer resin. The UV laser is used to draw a pre–programmed design on the surface of the photopolymer reservoir. The resin solidifies and forms a single layer of the desired object. The completed part is then washed with a solvent to clean wet resin from the surface. Supports are needed and are to be removed manually.

B. Application of pneumatic actuators within prostheses

In this study, we aim to create a pneumatic actuator with a SLA printer. A pneumatic actuator uses compressed air to move a piston inside a cylinder. Pneumatic actuators are used in a variety of situations, as they solely work based on compressed air. Compared to its hydraulic counterpart they offer less residue and an easier setup. For these reasons, pneumatic actuators could offer multiple applications in the medical world. There are numerous different pneumatic actuators, with a vast division in double-acting and single-acting cylinders. An advantage of creating a pneumatic actuator with AM, is the possibility to easily change the dimensions of the printed device to fit the specific requirements. In the field of biorobotics, for example in the use of prosthetics, this would be a great advantage, because the measurements of the device could be adjusted to the measurements of a human body. Furthermore, with the extra design freedom which AM provides, the used pneumatic piston-cylinder systems are not restricted to conventional circular cross-sections.

C. State of the art — 3D-printed pneumatics

Previous attempts on creating 3D-printed pneumatic actuators have mostly focused on flexible pneumatic actuators to create grippers [7], [8], or for rehabilitation devices [9]. Some studies describe the design of a 3D-printed non-flexible linear pneumatic actuator. Krause and Bhounsule created a double-acting pneumatic piston-cylinder system of mostly 3D-printed parts [10]. The parts were printed with a fused deposition modeling (FDM) printer using PLA material. In this actuator, some parts were reinforced to prevent failure. After post-processing steps to prevent leakage, it showed comparable strength and performance to commercially available actuators. A miniature double-acting 3D-printed pneumatic actuator was designed by Nall and Bhounsule [11]. This double-acting actuator was printed with a FDM printer using ABS as material. Just like in the study performed by Krause and Bhounsule, the piston was reinforced with a metallic part. After post-processing the inner cylinder wall with chemicals to create a smooth surface finish, the actuator showed comparable power-to-weight ratio to commercial actuators of the same size. Similar work to this study is the thesis of Martinez de Apellaniz Goenaga [12], who printed single-acting cylinders with different printing techniques — FDM, SLA and selective laser melting (SLM). He designed the cylinders for hydraulic use and studied the influence of the different printing methods on the slip-stick friction force when the piston starts moving. Furthermore he looked at the influence of post-processing steps on the friction force in the actuator. He found that SLA printing gave the best results, and processing the cylinder wall with a reamer lowered the friction force in the system. Besides AM, another fast prototyping option for the manufacturing of pneumatic actuators was studied by Groenehuis and Stramigioli [13]. They designed non-conventional pneumatic actuators which could be produced with laser-cutting technique. No published papers were found on 3D-printed pneumatic actuators where no post-processing steps were needed to prevent leakage. We also did not find any previous work on 3D-printing pneumatic actuators with a non-conventional cross-sectional shape.

D. Friction force in pneumatic actuators

When designing a pneumatic piston-cylinder system, one of the most important aspects is to prevent leakage. Applying a seal is essential to prevent leakage in a pneumatic actuator, but at the same time highly increases the friction within the system. Friction is always present in a pneumatic cylinder system [14], but the magnitude of the friction force depends on several aspects, which will be further discussed in Section II. When designing the 3D printed pneumatic actuator, we aim to prevent leakage while keeping the frictional forces to a minimum. This brings us to the objectives of this study.

E. Objectives

The goal of this thesis is to study the performance of a fully 3D-printed pneumatic actuator. The actuator will be created with AM without performing any post-processing steps to improve the performance. To analyse the performance of a 3D-printed piston-cylinder system, we focus on preventing leakage and at the same time maintaining a low friction force. In this study we test various models with different sealing mechanisms. This leads to the first two research questions.

- **RQ1** — How much leakage occurs in a 3D-printed piston-cylinder system and what influence do different sealing mechanisms have on the leakage?
- **RQ2** — How much dynamic sliding friction force is present in a 3D-printed piston-cylinder system and what influence do different sealing mechanisms have on this force?

Lastly, to show the full potential of 3D printing pneumatic actuators, we evaluate two designs of piston-cylinder systems with a non-circular cross-section.

- **RQ3** — Is it possible to create a pneumatic piston-cylinder system without its conventional cylindrical shape with AM and what design considerations influence the performance of such a 3D-printed non-conventional pneumatic actuator?

II. Methodology

In this section we will elaborate on our methods to provide answers to the posed research questions.

A. Circular actuators

Several cylinders were printed with a Formlabs 3 SLA printer, to test the influence of different sealing mechanisms on the performance of the pneumatic actuator.

1) Design of the pneumatic actuator: Two kinds of piston-cylinder systems exist — Single acting and double-acting cylinders. In this study we chose to design a single-acting cylinder, which can act as an air spring. For simplicity reasons, the cylinder is designed as one part; there is no separate cylinder head. The clearance between the piston and the cylinder in off-the-shelf cylinders is usually between 50 and $250\,\mu\mathrm{m}$ [15]. However, because AM has a limited surface finish, we chose for a higher clearance of $500\,\mu\mathrm{m}$ ($0.5\,\mathrm{mm}$) to prevent friction between the sliding interface of the piston and the cylinder wall. A separate piston is designed for each specific sealing mechanism, because each sealing requires specific groove measurements. The technical drawings for these designs can be found in Appendix F.

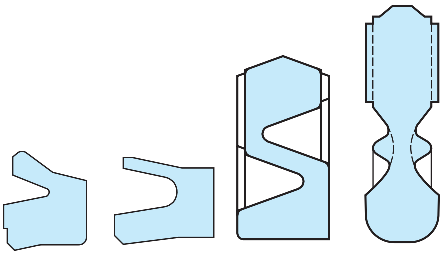

(a) (b) (c) (d)

Fig. 1: Single acting sealing mechanisms; NAP 310(a) [17] and NAPN(b) [18]. Double acting sealing mechanisms; PK(c) [19] and KDN(d) [20].

2) Sealing selection: The most common sealing shape is the O-ring — a cylindrical ring made from soft rubber. The X-ring is selected because according to a prominent manufacturer of sealing mechanisms, ERIKS, these rings are suitable for reciprocating sliding movements [16]. Furthermore two double-acting and two single-acting sealings are selected which promise a low sliding friction force. The cross-sections of these shapes are visualised in Figure 1. When selecting the sealing mechanisms, we aimed to find all sealings with the same outer diameter in order to compare them. We chose a standard bore size of $25\,\mathrm{mm}$. However, the X-ring was not available in an outer diameter of $25\,\mathrm{mm}$. We chose a X-ring with a diameter closest to the preferred $25\,\mathrm{mm}$; $25.7\,\mathrm{mm}$. In order to be able to make a comparison between the X-ring and the other sealing mechanisms, an extra O-ring was added to the test, also with an outer diameter of $25.7\,\mathrm{mm}$. Table I gives an overview of the selected sealings.

3) Piston grooves: For the O-ring and X-ring, the groove is designed in such a way that the sealings are squeezed by 10% when placed in the cylinder, which is within the compression range recommended by the manufacturer [21]. For the other shapes, the specific installation guides of the manufacturer were followed. These can be found in Appendix B.

B. Non-circular actuators

In order to show the full advantage of 3D printing pneumatic actuators, we designed actuators with non-circular cross-section. These actuators are not possible to manufacture using the conventional method [3]. An O-ring was used as a sealing mechanism, because this sealing mechanism can easily be shaped to the piston in order to provide the sealing which is needed. The first additional shape is a stadium-shape – a rectangle with semicircles at opposite ends, see Figure 2(b). The second shape resembles a kidney, see Figure 2(c). The stadium- and kidney-shaped piston-cylinder systems are tested with the same test setup as the circular cylinders. In order to create piston-cylinder systems which can be fairly compared, the non-conventional shaped cylinders are designed to have an equal cross-sectional surface area to the tested circular cylinder. At the same time we ensured that the inner perimeter of the cylinder is equal to the outer perimeter of the O-ring for proper sealing. The equations to determine the dimensions of the shapes can be found in Appendix C. We used an O-ring with an internal diameter of $22\,\mathrm{mm}$ and a cross-sectional diameter of $3.5\,\mathrm{mm}$ for these shapes. Table II gives an overview of the dimensions used for this test. The printed cylinders can be seen in Figure 3.

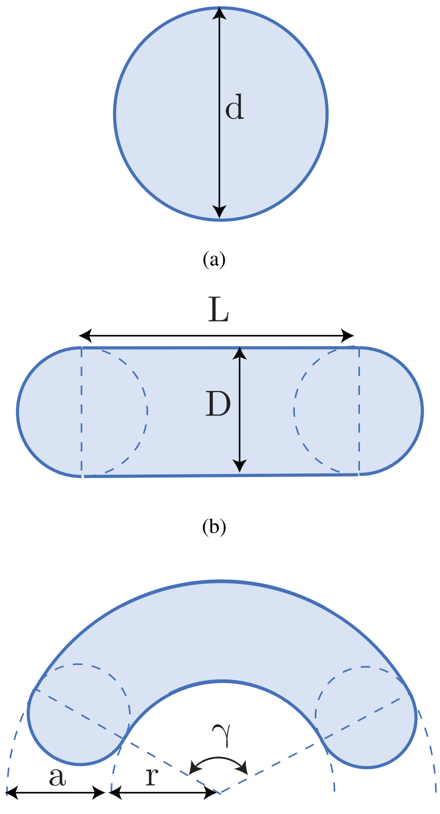

(a) (b) (c)

Fig. 2: The shape of the tested actuators: (a) A circular shape with diameter d, (b) a stadium shape with variables L and D, and (c) a kidney shape with variables a, r, and γ.

(a) (b)

Fig. 3: The sideview(a) and topview(b) of the 3D-printed pneumatic actuators with non-conventional cross-section.

TABLE I: Chosen sealing mechanisms. The standard sealing mechanism, the O-ring, is compared to an X-ring, two double-acting, and two single-acting sealing mechanisms.

Sealing mechanism	Single acting / Double acting	Material	Shore	Cylinder diameter
ERIKS O-ring	Double acting	NBR	70	25.7 mm
ERIKS X-ring	Double acting	NBR	70	25.7 mm
Parkside O-ring	Double acting	Unknown	70	25 mm
Merkel compactafdichting KDN	Double acting	NBR708	70	25 mm
Freudenberg Compactafdichting Airzet PK	Double acting	NBR	80	25 mm
Freudenberg groefringmanchet NAP310	Single acting	PUR994	80	25 mm
Freudenberg groefringmanchet NAPN	Single acting	NBR349	80	25 mm

TABLE II: Dimensions of the piston-cylinder systems

Shape	Dimensions O-ring	Defined variable		
Circular shape	18 mm × 3.5 mm	d		
		25 mm		
Stadium shape	22 mm × 3.5 mm	L	D	
		23.09 mm	14.30 mm	
Kidney shape	22 mm × 3.5 mm	r	a	γ
		6.08 mm	14.30 mm	$\frac{5}{9}\pi$ rad (100°)

C. Printing method

All actuators created during this research were printed with a Formlabs 3 SLA printer. Two factors were taken into account for this decision. Firstly, SLA has a relatively high surface finish. Martinez de Apellaniz Goenaga showed in his thesis that this results in a low friction force in 3D-printed hydraulic cylinders [12]. Secondly, we performed a preliminary research to assess the porosity of models produced by various printing methods. The Formlabs 3 printer demonstrated to be the best option of all available printers to the authors. This assessment can be found in Appendix A. The material used during this research is a Formlabs material: *ClearV4* [22]. We chose for a layer height of 100 µm to save printing time.

D. Experimental setup

1) Preparing the 3D-printed models: Prior to testing, the models are prepared with the following steps.

1) After washing and curing the 3D-printed models, the supports are removed manually.
2) The cylinder and air chamber are tapped with a M5 tap for the air inlet and a G1/8 tap for the pressure sensor.
3) The air inlet and pressure sensor are installed in the cylinder using Teflon tape to increase the sealing.
4) The sealing is installed on the piston.

After performing these initial preparations, the tests are executed.

2) Static leakage: Figure 4 shows a schematic overview of the test setup to measure leakage in the piston-cylinder system. The test for static leakage in the cylinder consists of the following steps:

1) When necessary, an offset value is applied to the pressure sensor ensuring a starting pressure of 0 MPa.
2) The manual control valve is properly closed, making the piston-cylinder system a closed system.
3) The piston is lubricated and placed in the cylinder.
4) The piston is moved to a fixed high-pressure position in the cylinder, ensuring equal starting pressure for each test model.
5) The pressure is measured for 20 min and transferred to the computer via LabVIEW.

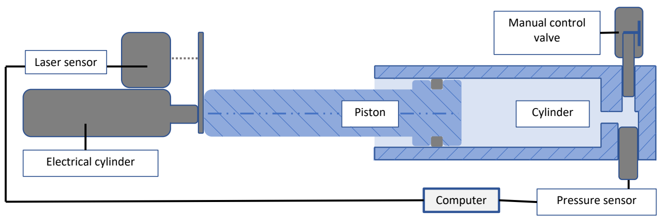

Fig. 4: Schematic overview of the leakage test

The pressure drop during the test can be interpreted as static leakage within the system.

3) Dynamic leakage: To measure the dynamic leakage within the system, the same test setup was used as for the static leakage test, see Figure 4. This test was designed to measure the dynamic leakage when the piston moves inside the cylinder. The test for dynamic leakage in the cylinder consists of the following steps:

1) When necessary an offset value is applied to the pressure sensor ensuring a starting pressure of 0 MPa.
2) The manual control valve is properly closed, making the piston-cylinder system a closed system.
3) The piston is lubricated if necessary and placed in the cylinder.
4) The piston is moved to the starting position. This starting position ensures that there will be some pre–tension on the sealing mechanisms during the test.
5) The piston is moved back and forth 38 mm for 200 times by the electrical cylinder. This process takes about 20 minutes.

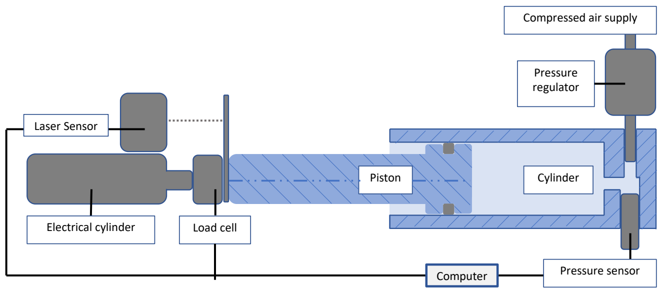

Fig. 5: Schematic overview of the friction test

6) The piston ends at its the starting position. The pressure is recorded during the entire test and transferred to the computer via LabVIEW.

With this method the pressure difference at a fixed position in the cylinder from the begin to the end of the test can be interpreted as the amount of dynamic leakage in the system.

4) Friction force: Due to non-linear behaviour modelling the dynamic friction force in a fluidic actuator remains a difficult task. The third test in this study is performed to determine the friction force occurring while using the pneumatic actuator. From previous work, we know the friction force is dependent on both the velocity in which the piston moves and the pressure on which it operates [14], [23]–[25]. Furthermore, specific properties of the actuator have an influence on the frictional force. According to Wassink et al, lip seal friction under constant speed sliding can be modelled as the sum of three physical components [24]:

- Viscous shear loss in the lubricant.
- Hysteresis losses due to roughness-imposed deformation of the seal material.
- Hysteresis losses due to deformation caused by varying intermolecular forces at the sliding interface.

In our study we use the same lubricant for each cylinder — Rocol Kilopoise 0001. The material and shape of the seal was varied during different test models. A schematic overview of the friction test can be seen in Figure 5. The test consists of the following steps:

1) When necessary an offset value is applied to the pressure sensor and load cell ensuring a starting pressure of $0\,\mathrm{MPa}$ and starting load of $0\,\mathrm{N}$.
2) The piston is lubricated if necessary and placed at the starting position.
3) The manual control valve is opened, making the piston-cylinder system an open system.
4) The pressure is set on 0.1, 0.3, 0.5 or $0.7\,\mathrm{MPa}$ using the pressure regulator. This pressure is controlled by the pressure regulator and will be kept constant during the test.
5) For each of these values, the piston is moved back and forth for ten times by the electrical cylinder.
6) The load cell measures the force acting on the piston provided by the electrical cylinder during the test. The pressure is measured during the entire test. Both values are recorded and transferred to the computer via LabVIEW.

A simplified free-body diagram of the piston in this test is shown in Figure 6. Forces in the y-, and z-direction are excluded for simplicity reasons. To find the friction force, F_F, we analyse the forces in the x-direction,

$$F_{LX} - F_F - F_p = m\frac{\mathrm{d}v}{\mathrm{d}t} \tag{1}$$

where F_{LX} is the force exerted by the load cell, F_p is the resultant force exerted by the gauge pressure, m is the mass of the piston, and v is the velocity of the piston. To calculate the friction force, we assume that the piston velocity is constant and therefore we can interpret the system as a steady-state system. The force F_p is calculated by multiplying the measured pressure (p) with the surface area of the tested cylinder (A)

$$F_p = p \cdot A. \tag{2}$$

The friction force can then be calculated

$$F_F = F_{LX} - F_p. \tag{3}$$

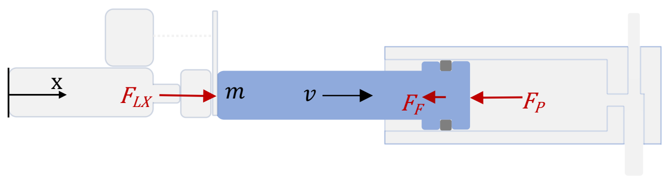

Fig. 6: A simplified free-body diagram of the piston in the friction test. Forces in the y-, and z-direction are excluded for simplicity reasons.

5) Test setup design: During this test the pneumatic cylinder is attached to a compressor via a pressure regulator (Festo MS4-LR-1/4-D7-AS), which provides a regulated pressure on the system. A picture of the test setup can be seen in Figure 7. During the tests, high forces up to $500\,\mathrm{N}$ are to be measured at pressures around $1\,\mathrm{MPa}$. To prevent deflexion in the system, we used an aluminium frame as a base to connect all different elements. An electrical cylinder (A, DSZY1-potentiometer), with its power source (B), is connected to the base. The laser sensor (C, Micro Epsilon optoNCDT) is connected at the other side of the electrical cylinder. The force sensor (D, Futek Miniature S-Beam Jr. Load Cell 2.0) is placed at the end of the electrical piston. The side of the force sensor which touches the piston of the tested model had a protruding element, which makes sure the piston stays aligned during the test (see Figure 7(b)). The force sensor pushes against the piston of the 3D-printed cylinder (F). A part was designed to align the test element during the tests, see Figure 7(c). The pressure sensor (E, SensorTechnics CTU8000), measures the pressure during the tests. The manual control valve (G, Festo Shut-off valve) is fixated on the base with a connecting part (Figure 7(d)), to prevent movement of the connecting elements during the test. The sensors are connected via LabVIEW to a computer (I). To counteract the high axial forces and prevent undesired tensions in the system, both sides are strengthened by the aluminium pillars which can be seen in Figure 7(a). Appendix D explains the steps taken to finalise our test rig.

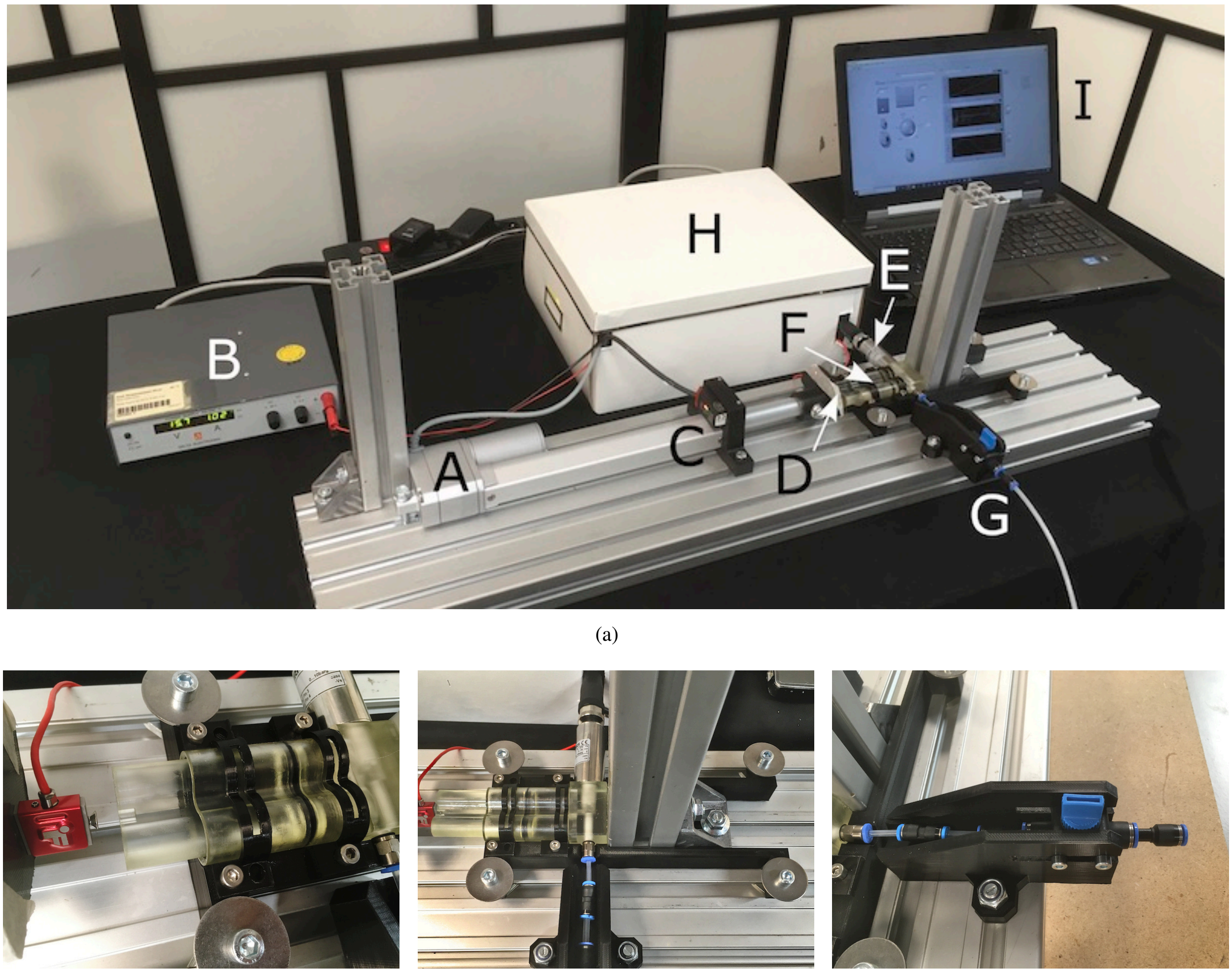

(a)

(b) (c) (d)

Fig. 7: A picture of the experimental test setup consisting of an electrical cylinder (A) with its power source (B), a laser sensor (C), a force sensor (D), a pressure sensor (E), the 3D-printed test model (F), an air inlet with manual control valve (G), a box with electronical components (H) connecting the sensors via LabVIEW to a computer (I).

E. Data analysis

1) Static leakage: To adequately visualise the results of the static leakage test, the data required little post–processing. Merely a sliding averaging window and sampling of the data was applied.

2) Dynamic leakage: Ideally we would analyse the difference in pressure at the starting position of the cylinder, from the beginning of the test up until the end of the test as a metric for the dynamic leakage. However, due to an overshoot of the electrical cylinder this is not possible. To analyse of the dynamic leakage, we chose to find the pressure at a specific point in the cylinder and check how this pressure behaves over time. In order to find this pressure, the data from the laser sensor was combined with the data from the pressure sensor. We defined a variable α as the position in the cylinder where we want analyse the pressure. This variable slightly differs per test model, to ensure equal starting pressure for every model. The laser sensor provides highly accurate values (in mm) up to three decimals. For the analysis of the dynamic leakage all pressures were selected where the laser sensor gave the value of $\alpha-0.02\,\mathrm{mm}$ to α+$0.02\,\mathrm{mm}$.

3) Friction force: A visualisation of the friction force at $0.1\,\mathrm{MPa}$ can be seen in Figure 8. As a metric to compare the dynamic sliding friction force of the different models, we chose to take the difference of the friction force of the extending stroke to the friction force on the retracting stroke indicated by the black arrow in the figure. We call this metric the friction force range. Therefore, we have to take into account that this results in measuring the average friction force for one entire stroke. Other literature might observe both the retracting and extending stroke individually, which would result in about half the friction force range. For each of the ten movement cycles, the friction force range is determined. To assess the variation between these ten tests we calculate the standard error between the different runs.

4) Repeatability of the test results: In order to find the variation within our measurements, a repeatability test was performed on one of the models for all the tests performed. This consisted of two steps. Firstly, we ran the measurements three times in a row, without changing the connections of

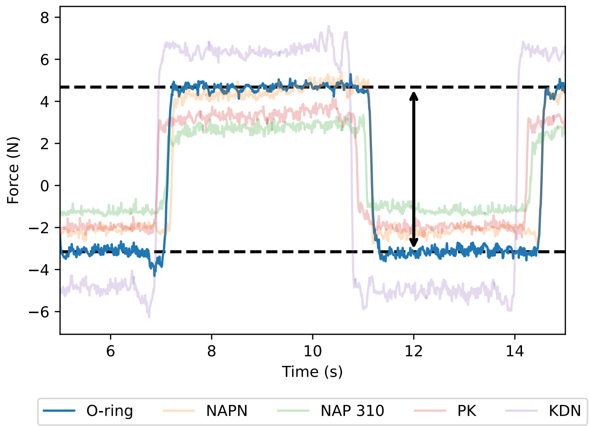

Fig. 8: The friction force range definition at $0.1\,\mathrm{MPa}$

the air inlet and pressure sensor. Secondly, the air inlet and pressure sensor were disconnected and reconnected prior to taking the test. Again, the test was performed three times, while reconnecting the model every time, to find the variation within our results.

III. Results

A. Circular actuators

1) Static leakage: Figure 9 shows the result of the static leakage test of the sealing mechanisms with the diameter of $25\,\mathrm{mm}$. The pressure at the start of the test was $0.55\,\mathrm{MPa}$ in all cases. All models were able to keep the $0.55\,\mathrm{MPa}$ inside the system, except the model with the NAP310 sealing, which lost all the pressure during the test. Figure 10 can be used to distinguish between the remaining sealings, where 10(a) shows the static leakage in the $\varnothing 25\,\mathrm{mm}$ cylinder and 10(b) shows the static leakage in the $\varnothing 25.7\,\mathrm{mm}$ cylinder. Besides the NAP310 sealing, the other sealings lost a pressure with a maximum $0.014\,\mathrm{MPa}$ during the entire test (under $\pm 3\%$).

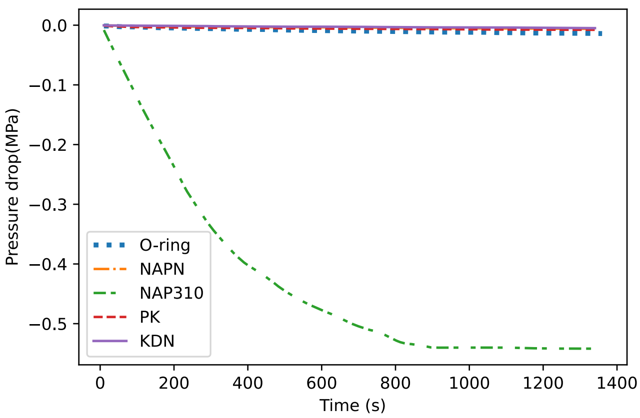

Fig. 9: Static leakage in the $\varnothing 25\,\mathrm{mm}$ cylinder

2) Dynamic leakage: During this test the cylinder was placed at the same starting position during every test. However, it turned out to be challenging to reach exactly the same starting position for every test. Each test therefore had a slightly different value of α in order to create a valid comparison between the different models. These values can be found in Table III. Analysing Figure 11(a), we can see that the NAP310 sealing does not keep the system pressurised, similar to the static leakage results. The pressure at the measured position in the cylinder at the start of the test is slightly above $0.8\,\mathrm{MPa}$. After 200 movement cycles (with a duration of 20 minutes), the pressure in this model is decreased to $0.5\,\mathrm{MPa}$ at this position. When observing the dynamic leakage in the $\varnothing 25\,\mathrm{mm}$ cylinder, the best performing sealings are the NAPN- and the KDN-seal. The O-ring and the PK sealing both show a pressure loss of approximately $0.1\,\mathrm{MPa}$ during the dynamic pressure test. Figure 11(b) shows that both the X-ring and O-ring in the $\varnothing 25.7\,\mathrm{mm}$ cylinder hold the pressure during the entire test.

TABLE III: Values of α for each sealing

Test model	α
$\varnothing 25\,\mathrm{mm}$ cylinder	
O-ring	$37.7\,\mathrm{mm}$
NAPN	$38.0\,\mathrm{mm}$
NAP310	$37.7\,\mathrm{mm}$
PK	$37.8\,\mathrm{mm}$
KDN	$37.7\,\mathrm{mm}$
$\varnothing 25.7\,\mathrm{mm}$ cylinder	
O-ring	$37.7\,\mathrm{mm}$
X-ring	$37.7\,\mathrm{mm}$

3) Friction force: The friction force of one total movement cycle was evaluated on four different pressure levels; 0.1, 0.3, 0.5, and $0.7\,\mathrm{MPa}$. Figure 12(a) shows the friction force range for the different sealings in the $\varnothing 25\,\mathrm{mm}$ cylinder and Figure 12(b) shows the friction force range in the $\varnothing 25.7\,\mathrm{mm}$ cylinder. The error bars around each mean friction force range indicates the standard error over ten movement cycles for each model. All the sealings show an increase in friction force with increasing pressure. The sealing with the highest friction force is the X-ring, showing a friction force range of $9\,\mathrm{N}$ at a pressure of $0.1\,\mathrm{MPa}$, whilst this increases up to almost $30\,\mathrm{N}$ at a pressure of $0.7\,\mathrm{MPa}$. The sealings with the lowest friction force are the single-acting NAP310 sealing and the double-acting PK sealing. One of the sealing mechanisms shows a friction force which is almost independent of the pressure — the friction force of the double-acting KDN sealing only increases a small amount with an increase of pressure. This sealing resulted in a friction force range of $11.2\,\mathrm{N}$ at a pressure of $0.1\,\mathrm{MPa}$ and at the highest tested pressure level of $0.7\,\mathrm{MPa}$ the friction force range increased to $13.4\,\mathrm{N}$.

4) Repeatability: The repeatability tests were performed with the O-ring sealing on the $\varnothing 25.7\,\mathrm{mm}$ cylinder. The results are shown in Figures 13, 14, and 15 for the static leakage test, the dynamic leakage test and the friction force test respectively. The previously tested models were added in the background for comparison. Figures 13(a), 14(a), and 15(a) show the results where the test was simply rerun and Figures 13(b), 14(b), and 15(b) show the results where the model was reconnected before every test. Looking at Figure13(a), we can observe that the differences measured in the static leakage test fall within the uncertainty of the data, except for

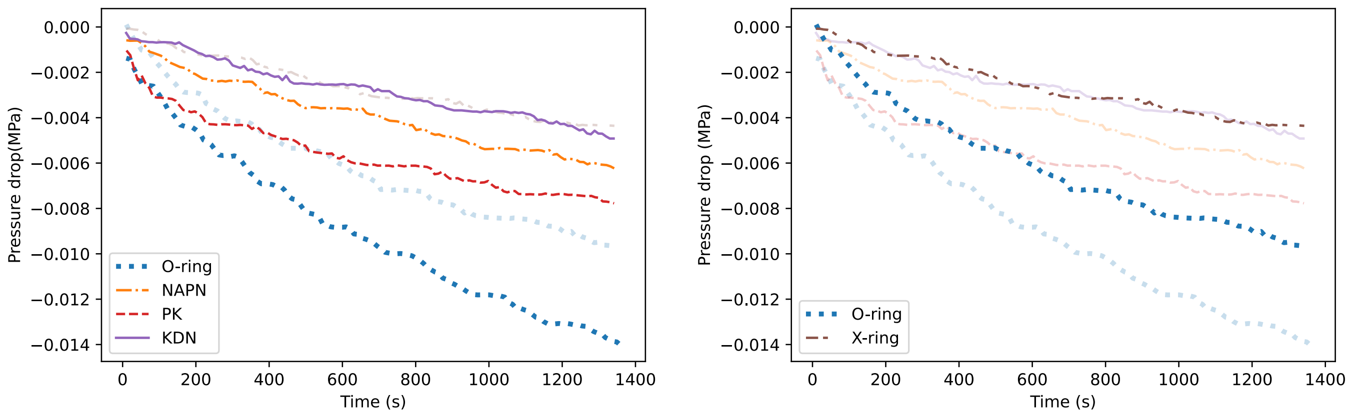

(a) (b)

Fig. 10: Static leakage of sealings in the circular actuators of $\varnothing 25\,\mathrm{mm}$(a) and $\varnothing 25.7\,\mathrm{mm}$(b)

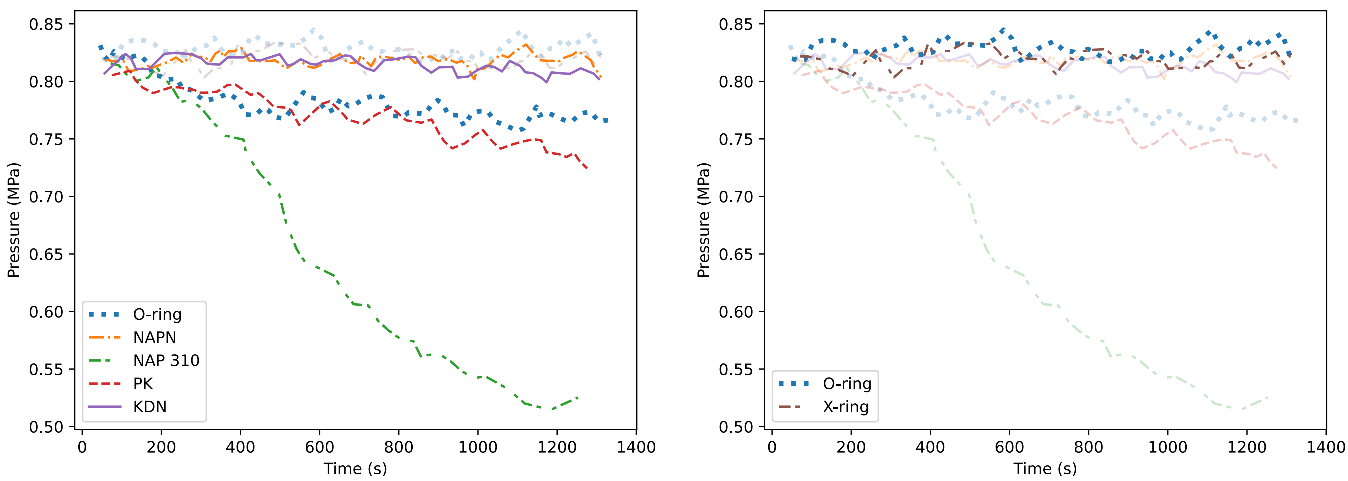

(a) (b)

Fig. 11: Dynamic leakage of sealings in the circular actuators of $\varnothing 25\,\mathrm{mm}$(a) and $\varnothing 25.7\,\mathrm{mm}$(b)

the NAP310 sealing, which was left out of this figure for better comparison. The results of the dynamic leakage and friction force range are comparable for each repeatability test.

B. Non-circular actuators

1) Static leakage: The results of the static leakage test with the non-circular cylinders are illustrated in Figure 16. We can observe that the more conventional cylindrical shape performed best in the static test with a pressure drop of approximately $0.01\,\mathrm{MPa}$ for the duration of the test with a starting pressure of $0.55\,\mathrm{MPa}$ (1.8%). The stadium-shaped model lost double the amount of pressure — $0.02\,\mathrm{MPa}$ over the duration of the test (3.6%). The kidney-shaped model dropped from $0.55\,\mathrm{MPa}$ to $0.49\,\mathrm{MPa}$, and thus dropped $0.06\,\mathrm{MPa}$ of pressure during the test (10.9%).

2) Dynamic leakage: To ensure a valid comparison of the non-cylindrical models to the cylindrical model, values of α were hand-picked. The position in the cylinder was chosen where the starting pressure of the test is the same for all three models. The values of α which are used in the data analysis are shown in Table IV. The results of the dynamic leakage of the non-cylindrical piston-cylinder systems can be found in Figure 17. The pressure in the circular shape remains most constant over time. The stadium shape showed a leakage of approximately $0.1\,\mathrm{MPa}$ after 200 movement cycles — the pressure decreased from $0.7\,\mathrm{MPa}$ to $0.6\,\mathrm{MPa}$ at the chosen position in the cylinder. The kidney-shaped actuator produced a lot of dynamic leakage, as during the test the pressure at the measuring position in the cylinder decreased from $0.7\,\mathrm{MPa}$ to merely $0.1\,\mathrm{MPa}$.

TABLE IV: Values of α for each shape

Test model	α
Circle	$36.7\,\mathrm{mm}$
Stadium	$38.5\,\mathrm{mm}$
Kidney	$39.3\,\mathrm{mm}$

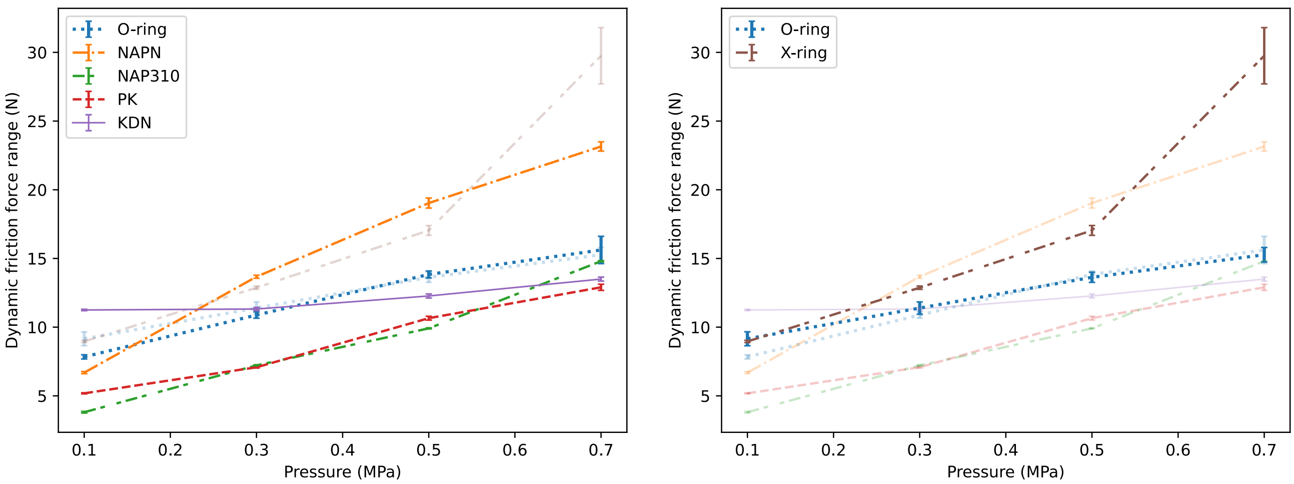

(a) (b)

Fig. 12: The mean friction force dange of sealings in the circular actuators of $\varnothing 25\,\mathrm{mm}$(a) and $\varnothing 25.7\,\mathrm{mm}$(b) at a pressure of 0.1 to $0.7\,\mathrm{MPa}$

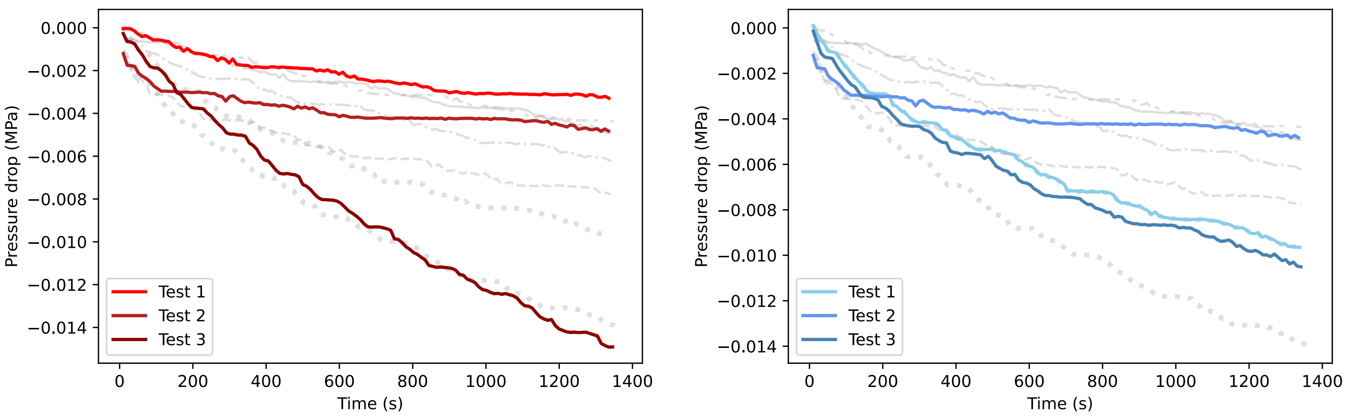

(a) (b)

Fig. 13: The repeatability results of the static leakage test where (a) the test was rerun without any changes in the connections and (b) the model was reconnected prior to taking the tests

3) Friction force: During the friction force tests of the varying cross-sectional shaped cylinders, the placement of the O-ring in the piston groove was less stable in the non-cylindrical shapes compared to the cylindrical model. When increasing to higher pressures, the O-ring extrudes. In Figure 18 we can see the O-ring extruding in the clearance between the piston and the cylinder. For this reason the friction force was measured at increments of $0.1\,\mathrm{MPa}$ instead of the pre–defined pressure values. Interestingly, the kidney-shaped model could withstand a higher pressure compared to the stadium model before extruding. The stadium-shaped and the kidney-shaped models were tested up to a pressure of $0.3\,\mathrm{MPa}$ and $0.4\,\mathrm{MPa}$ respectively. Analysing Figure 19, we can see that the kidney-shaped actuator has the highest friction force range. Compared to the other models, the kidney shape showed more deviation between the different pressure levels. The friction force range was $13.6\,\mathrm{N}$ at $0.1\,\mathrm{MPa}$, $21.2\,\mathrm{N}$ at $0.2\,\mathrm{MPa}$, $19.3\,\mathrm{N}$ at $0.3\,\mathrm{MPa}$, and $21.3\,\mathrm{N}$ at $0.4\,\mathrm{MPa}$. The friction force of the stadium shape is more comparable to the circular-shaped actuator, it is only slightly higher than the circular-shaped actuator at all tested pressure levels.

IV. Discussion

A. *3D printing pneumatic actuators*

In this study we have shown the possibility of producing a pneumatic actuator with AM without performing any post–processing steps and have evaluated their performance based on leakage and friction. Generaly speaking, the results demonstrate that most sealings are functional in 3D printed pneumatic actuators, on which we will elaborate in the following subsections. Furthermore, we have shown that it is possible to create custom 3D-printed pneumatic actuators with various shapes, and with this opening the door to more design freedom in actuators.

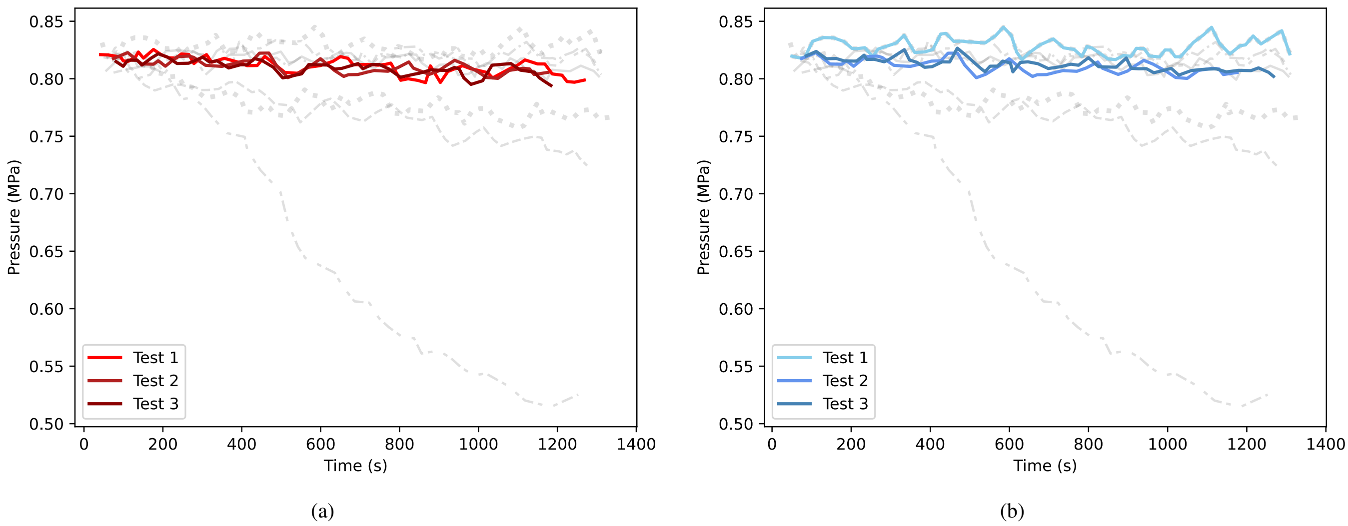

Fig. 14: The repeatability results of the dynamic leakage test where (a) the test was rerun without any changes in the connections and (b) the model was reconnected prior to taking the tests

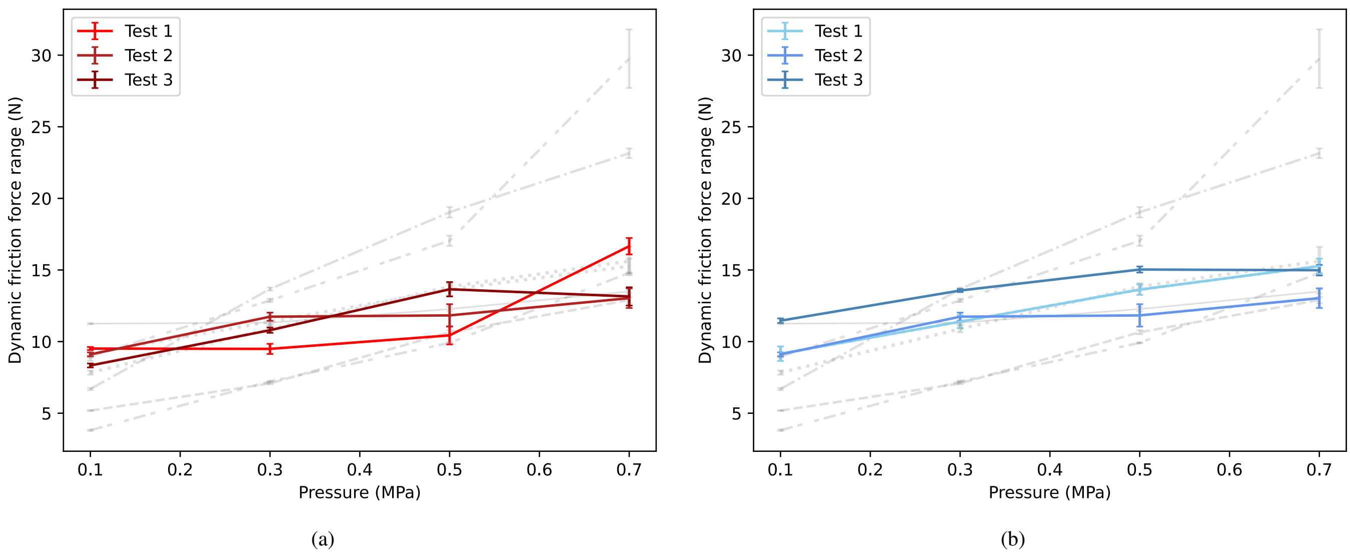

Fig. 15: The repeatability results of the friction force test where (a) the test was rerun without any changes in the connections and (b) the model was reconnected prior to taking the tests

B. Sealing mechanisms

1) Trade-off: leakage vs friction force: Combining the results on leakage in the system and measured friction force, we can observe that choosing the right sealing mechanism remains a trade-off between the leakage occurring within the piston-cylinder system and the friction force acting in the system. We see an overall trend in our data of high-leakage sealing mechanisms showing low frictional force. At the same time, the sealings showing the lowest pressure drop during the leakage tests have a relatively high friction force.

2) Single-acting sealings: For this study we tested two single-acting sealings, which both have the shape of a cup, see Figure 1(a) and 1(b). At low pressures, only a small part of the lip touches the cylinder wall, which results in a low friction force. However, at higher pressures, the lip is pushed sideways and the friction force rapidly increases when higher pressures are applied. Analysing Figure 12, we see that the NAPN sealing shows a large increase of the friction force at high pressures compared to the other sealings. Similar to the NAPN sealing, the NAP310 is also a single-acting sealing in the shape of a cup. When analysing Figure 11(b) and Figure 9 it can be observed that in both cases the NAP310 sealing mechanism is the sealing mechanism which leaks the most of all tested sealing mechanisms. The shape of this sealing mechanism can be seen in Figure 1(a). Compared to the other 'cup-shaped' sealing, the NAPN in Figure 1(b), a smaller part of the sealing touches the cylinder wall when the piston is placed inside the cylinder. We expect that the tolerance of our

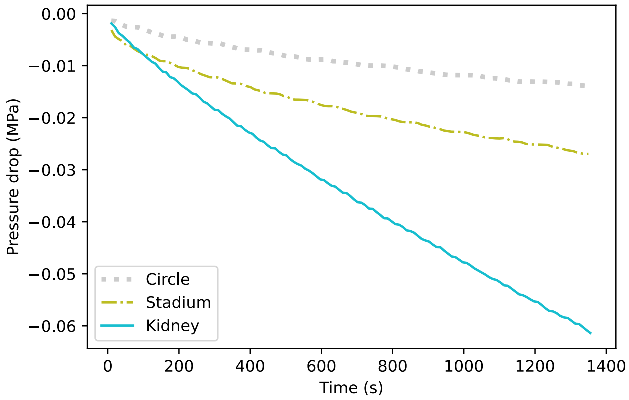

Fig. 16: Static leakage in the cylinders with non-circular cross-section

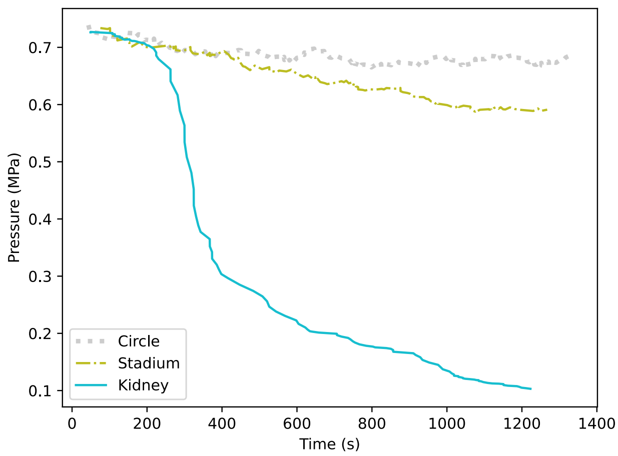

Fig. 17: Dynamic leakage in the cylinders with non-circular cross-section

printing method is too high for this sealing to work properly. For future use of these kind of single-acting sealings, we need to take into account that two of these seals have to be used simultaneously to seal a double-acting piston-cylinder system — doubling the frictional force compared to the other tested sealings.

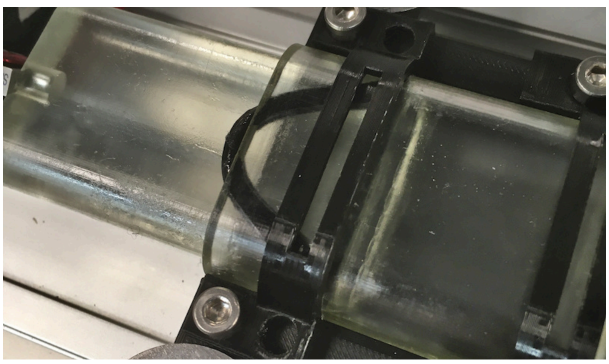

Fig. 18: The O-ring extrudes at pressures from $0.4\,\mathrm{MPa}$

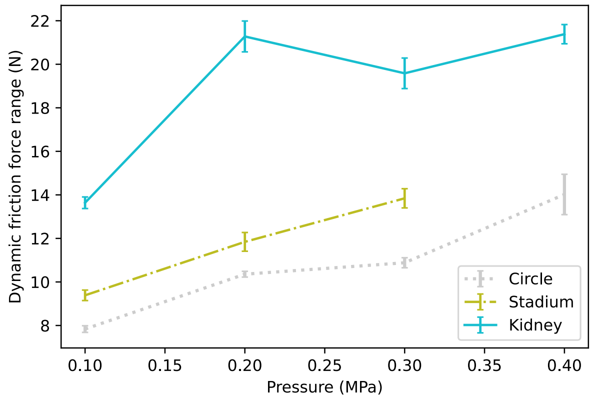

Fig. 19: Friction force in the cylinders with non-circular cross-section

3) Double-acting sealings: Two O-rings were used during testing to match the slightly different measurements of the X-ring and the other tested sealings. However, to find matching O-rings, we had to use O-rings from different brands. The $\varnothing 25\,\mathrm{mm}$ O-ring is from the brand Parkside. The $\varnothing 25.7\,\mathrm{mm}$ O-ring is from ERIKS, a company more specialised in pneumatic sealings. The difference between these two rings can be observed in both the dynamic and static leakage test, where the O-ring from ERIKS performs best in both tests. Concerning friction force, the two O-rings show equal results. For proper sealing, the authors would advise to use high-quality sealings produced by specialised companies for future actuator designs.

Looking at the results from the X-ring, we observe that it performs adequately on both dynamic and static leakage. This sealing mechanism proved to be one of the most leakage-free sealings we tested. However, we see a high increase in tested friction force at higher pressures. The shape of the sealing can explain this, as the X-ring has two area's simultaneously sealing the piston-cylinder clearance. This ensures a low possibility for air to escape, but comes with a higher friction force. An added advantage of the X-ring is that, because of the X shape, the possibility of the ring rotating in its groove is very low which limits the possibility of damage [16].

Our results show that the double-acting PK sealing is the sealing mechanism with the lowest friction force, when little leakage in the system is acceptable. For all tested pressure levels, the sealing shows a low frictional force. Looking at the static leakage test, the mechanism works very well. Only during the dynamic test the cylinder lost some pressure.

The last sealing we would like to discuss is the double-acting KDN sealing. This sealing was relatively difficult to install due to its shape. However, When comparing the leakage results (Figure 11(a) and 10(a)) and the friction results (Figure 12(a)), the KDN looks the most promising sealing mechanism for overall use. It shows, together with the NAPN sealing and the X-ring, the least amount of leakage during our tests. However, unlike the NAPN sealing and the X-ring, it does not show a high increase in friction force with increasing pressure. This makes the KDN sealing the most suitable of the tested sealings for high-pressure situations.

C. Non-circular shapes

1) Stadium shape: The first non-circular shape tested is the stadium shape. Compared to the circular-shaped actuator, the stadium-shaped model only showed a slightly larger pressure loss. We think this is mainly due to movement possibilities of the O-ring in the piston groove. On the flat side of the stadium piston, the O-ring does not have much pre–tension, as the circular O-ring tends to stay in its circular shape. Furthermore, the cylinder was designed with a higher clearance compared to conventional actuators as described in Section II, giving more room for the O-ring move or rotate inside the piston groove. The high pressure in the cylinder during the friction test caused a shear stress in the cylinder wall, which created a slight deformation of the cylinder wall. This further increased the possibility for the O-ring to extrude. Therefore the test could only be performed up to $0.3\,\mathrm{MPa}$. When comparing the friction force results of the stadium shape to the circular piston-cylinder system in Figure 19, we can see that the friction force of the stadium shape is slightly higher with all pressure levels compared to the circular shape. This was expected, because this shape has a larger perimeter presumably leading to an increase in friction.

2) Kidney shape: The kidney-shaped model could be tested up to a pressure of $0.4\,\mathrm{MPa}$. Even though a lower performance was measured in the kidney-shaped actuator compared to the circular one, we did show the possibility to 3D-print a pneumatic actuator with a non-circular cross-section. One of the main difficulties of the kidney shape, is that the used O-ring is circular shaped and will not naturally follow the piston groove. The form-closure of the cylinder wall is important to bring the O-ring in pre–tension. During the friction test, we could see the O-ring rotating inside the groove. We think that due to the form-closure, a difference in shear stress arises in the O-ring during the movement of the piston, making the O-ring rotate. During both the dynamic leakage and friction test we observed rotation of the O-ring in its groove. Firstly, the results for dynamic leakage in Figure 17 curiously shows a large pressure drop between 300 and 350 seconds, which can be explained by the rotation of the O-ring observed during that time interval. Secondly, as can be seen in Figure 19, the dynamic friction force range of the kidney-shape shows an outlier at a pressure of $0.2\,\mathrm{MPa}$. During this test we observed the O-ring rotating in its groove. We hypothesize this is the result of a large clearance gap, giving the O-ring too much space to move.

3) Reducing the clearance: As discussed in the previous subsections, the main problem of the actuators with non-conventional shapes seemed to be the rotation and extrusion of the O-ring. Two possible improvements could solve this. The first potential improvement is using an X-ring instead of an O-ring, because these rings are suitable to prevent rotation of the sealing [16]. The second improvement is decreasing the clearance gap between piston and cylinder. We have performed an additional folow-up test to assess this second proposition with two extra models on our test rig. For the two non-circular shapes, the clearance was reduced from $0.5\,\mathrm{mm}$ ($500\,\mu\mathrm{m}$) to $0.2\,\mathrm{mm}$. The same method was used to perform the tests as described in Section II. Figure 20 shows the results of the follow-up tests performed with these models. The friction results showed two advantages of lowering the clearance (Figure 20(c)). Firstly, higher pressure levels could be reached until the O-ring extruded. Secondly, both models showed a lower friction force compared to the corresponding models with a clearance of $0.5\,\mathrm{mm}$.

Unfortunately, the stadium-shape showed more leakage in this follow-up test. We think this is due to damages on the connector threads. However, when pointing our attention to the results for the low clearance kidney-shape, our expectations are exceeded. we can see an improvement for all the three tests performed on this model. Especially the results for the dynamic leakage test are promising, where the leakage was reduced to almost zero over the 200 runs of which the experiment consisted. This confirms the feasibility of 3D printing different shaped actuators and at the same time shows its huge potential.

D. Comparing to the state of the art

No previous work was found which compared the leakage and dynamic sliding friction force of 3D-printed pneumatic actuators. Furthermore we found no previous work on comparing different sealing options with 3D-printed pneumatic actuators. The 3D-printed linear pneumatic actuators by Krause and Bhounsule [10] and Nall and Bhounsule [11] were evaluated on the control of the actuator. Martinez de Apellaniz Goenaga evaluated pneumatic actuators created with different printing techniques on friction force [12]. As there is not much available literature to compare our results with, we tried to compare our results with commercial actuators.

Tran and Yanada evaluated the dynamic sliding friction force of commercial pneumatic actuators of $25\,\mathrm{mm}$ bore size in their study [14] at different pressure levels and different velocities. To compare the friction force found in this study to commercial actuators we calculated the velocity of our piston during one of the tests. At a pressure of $0.3\,\mathrm{MPa}$ the velocity of the extending stroke was $-11.4\,\mathrm{mm\,s^{-1}}$ and the velocity of the retracting stroke was $7.8\,\mathrm{mm\,s^{-1}}$. The corresponding results of Tran and Yanada for these velocities and pressure levels are shown in Table V. We can conclude that our 3D-printed actuator resulted in a friction force of the same order of magnitude as the commercially available actuators based on this comparison. Our 3D-printed actuator even shows less friction force, but this is probably due to the difference in actuator design. Tran and Yanada studied a double acting sealing, which has an extra rod seal, next to the piston seal. Our model only contains one piston seal.

E. Limitations

In this study we used sensors which have a range of 0-$500\,\mathrm{N}$ and $0-1\,\mathrm{MPa}$ for the force sensor and pressure sensor respectively. However, because we used the difference between these two sensors to determine our results, they are of a smaller order of magnitude. The pressure sensor can have an error up to 1% [26]. When there is a minimal misalignment in the system, the force sensor can show an error up to 1.5% (see

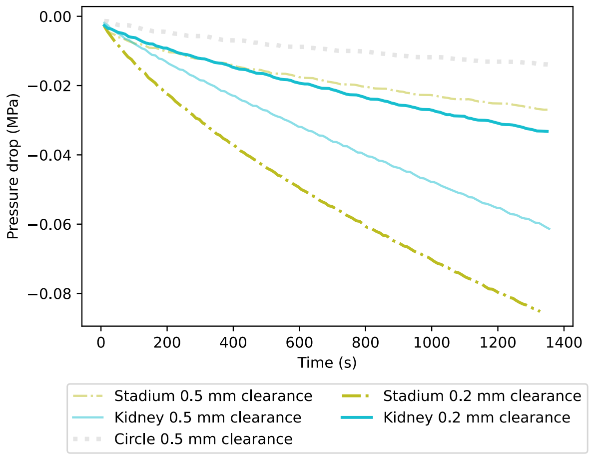

(a) The static leakage with lower clearance

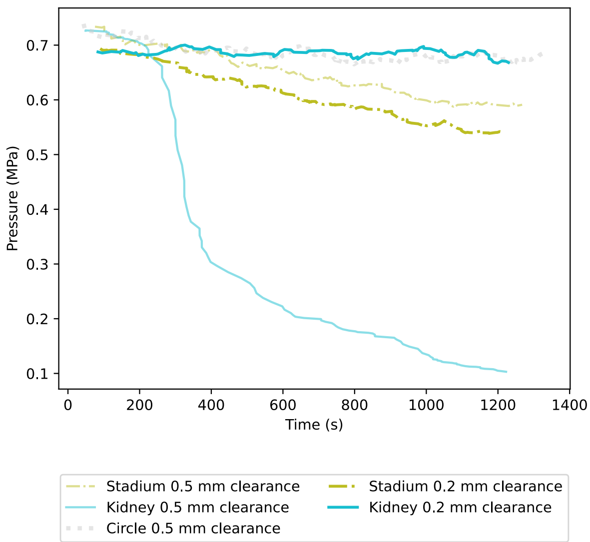

(b) The dynamic leakage with lower clearance

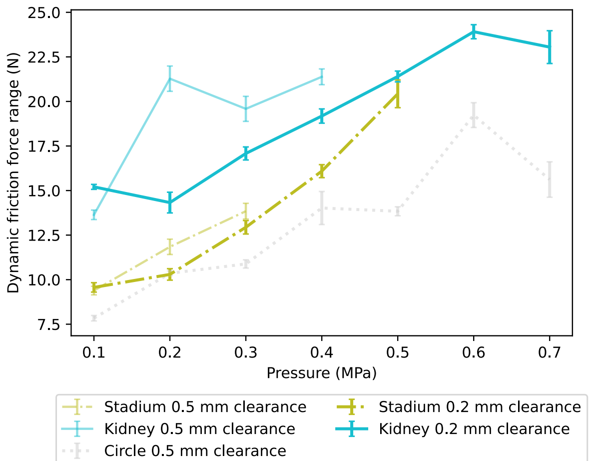

(c) The friction force with lower clearance

Fig. 20: Test results of the tests for pistons with a lower clearance

TABLE V: Found friction force compared to commercially available actuators at 0.3 MPa

Model	Stroke	Friction force	velocity
3D-printed actuator	Extending	7.8 N	$0.011\,\mathrm{m\,s^{-1}}$
	Retracting	3.4 N	$0.0078\,\mathrm{m\,s^{-1}}$
	Entire	11.2 N	
Standard actuator [14]	Extending	7 N	$0.01\,\mathrm{m\,s^{-1}}$
	Retracting	8 N	$0.005\,\mathrm{m\,s^{-1}}$
	Entire	15 N	

Appendix E). However, these relatively small errors for each sensor are a high percentage of our total test results. To further decrease the error in the force measurement, a universal joint could be used to ensure only axial forces to be measured, like Belforte used in their test setup [23].

Furthermore, the velocity of the electrical cylinder which we chose in the test turned out to be force-dependent. This can have an influence on the measurements of the friction force, because the friction force is dependent on the piston velocity. Our friction force was measured at relatively small velocities of around $0.01\,\mathrm{m\,s^{-1}}$, where extra Stribeck friction can be measured next to the Coulomb friction [14]. For future studies, we would advise to use an electrical cylinder in which the velocity of the actuator is not dependent on the force which it should provide, similar to Belforte et al. used in their study about sealing frictional force in 2013 [25]. Another option is to use a hydraulic cylinder to actuate the tested cylinder, like Tran&Yanada [14] and Belforte et al. [23] did in their studies for dynamic sliding friction force in commercial pneumatic actuators in 2013 and 2003 respectively.

F. Future research

Studies to further improve the performance of 3D-printed pneumatic actuators could focus on studying the effect of printing settings like layer height on the friction force, because this might influence the surface roughness of the cylinder wall and therefore the sealing performance and friction force within the actuator. The chosen sealings are all designed to work best on a maximum material roughness of $4.0\,\mu\mathrm{m}$. However, the roughness of 3D-printed materials is much higher. To save time during the printing process, the models used in this study were printed with a layer height of $100\,\mu\mathrm{m}$. The most precise printing layer height with the used printer is $25\,\mu\mathrm{m}$.

Another method to lower the surface roughness is by performing post–processing steps on the cylinder wall. Martinez de Apellaniz Goenaga showed in his study that processing the cylinder wall with a reamer decreases frictional forces in 3D-printed pneumatic actuators [12]. However, during this study only cylindrical actuators were compared. Reaming the cylinder wall will be more difficult as the geometry complexity of the actuator increases.

In this study we took the first steps in 3D-printing non-cylindrical pneumatic actuators. As a next step in reaching the goal of creating leakage-free and customised actuators, research could focus in finding sealing options which can be pre–formed to the desired shape. Also the option of printing the sealing mechanism wit multi-material printing would be interesting to study, although this is not possible when printing with SLA. A prior study on printing the sealing has been done by Siegfahtr et al. in 2020 [27].

To learn how the pneumatic cylinders and sealings would perform in long term, a durability test should be performed. In addition to these suggestions to further improve the performance of the 3D-printed cylinders, as we showed 3D-printed cylinders are suited to be incorporated into real applications.

V. Conclusion

In this study we presented the design of a fully 3D-printed pneumatic actuator. The design required no post-processing steps on the cylinder wall of the pneumatic cylinder. We presented a method to validate the performance of the models, concerning leakage in the pneumatic actuator and dynamic sliding friction force. To answer **RQ1** and **RQ2**, we tested seven different sealings in 3D-printed pneumatic actuators. We showed choosing a suitable sealing mechanism for the application seems to be a trade-off, where sealings with the smallest pressure drops showed the highest frictional force.

For low-pressure applications up to $0.15\,\mathrm{MPa}$ the single-acting NAPN sealing provides the lowest tested friction force, while preventing leakage in a dynamic and static situation. For a pressure of $0.1\,\mathrm{MPa}$, $6.7\,\mathrm{N}$ friction force for the extension stroke and retracting stroke together was measured. In the mid-range of $0.15\,\mathrm{MPa}$ to $0.3\,\mathrm{MPa}$, the O-ring gives the best friction results. For higher pressure situations above $0.3\,\mathrm{MPa}$, the double-acting KDN sealing shows the most promising results. The friction force for this seal remains fairly constant with increasing pressure. From a total friction force range of $11.2\,\mathrm{N}$ at $0.1\,\mathrm{MPa}$ to $13.5\,\mathrm{N}$ at $0.7\,\mathrm{MPa}$. In situations where a low friction force is desired and a small dynamic leakage is acceptable, the double-acting PK is an adequate option. This sealing resulted in a friction force of $5.2\,\mathrm{N}$ at $0.1\,\mathrm{MPa}$ which increased to $12.9\,\mathrm{N}$ at the highest tested pressure level of $0.7\,\mathrm{MPa}$.

Furthermore, in this study the first steps were shown towards a piston-cylinder system with a non-cylindrical cross-section, answering **RQ3**. Although creating a complete leakage-free actuator was not achieved yet, it turned out to be possible to 3D-print a stadium-shaped piston-cylinder system with only minimal dynamic leakage. A pressure drop of $0.75\,\mathrm{MPa}$ at the start of the test to $0.6\,\mathrm{MPa}$ after 200 runs was measured during the dynamic test and the frictional force was comparable to a cylindrical system. Besides a stadium-shaped 3D-printed cylinder, the design of a kidney-shaped actuator is presented in this study. Initially the results of this model showed a lot of leakage, however, after retesting with minor adjustments this issue was solved. The kidney-shaped single-acting cylinder, although a higher friction force was measured compared to the other models, worked up to a pressure of $0.4\,\mathrm{MPa}$ and with minor adjustments even to the maximum tested pressure level of $0.7\,\mathrm{MPa}$. This opens the world to customised pneumatic actuators, enabling geometry improvements in applications such as prostheses or orthoses.

VI. Acknowledgements

The authors would like to thank Spidiron van Veldhove, Jan van Frankenhuyzen and Reinier van Antwerpen and Damian de Nijs for their help producing the test models. Also, we would like to thank Jos van Driel for his technical support while creating the test rig. Without him it would not have been possible to thoroughly test the designs.

VII. Data availability

The full data of the tests performed in this study, together with the python scripts to process the data is available via GitHub at https://github.com/EvaZillen/3D-printed-pneumatic-actuator.

References

[1] M. Attaran, "The rise of 3-D printing: The advantages of additive manufacturing over traditional manufacturing," *Business Horizons*, vol. 60, no. 5, pp. 677–688, 2017. DOI: 10.1016/j.bushor.2017.05.011. [Online]. Available: https://www.sciencedirect.com/science/article/abs/pii/S0007681317300897

[2] R. Bogue, "3d printing: The dawn of a new era in manufacturing?" *Assembly Automation*, vol. 33, 09 2013. DOI: 10.1108/AA-06-2013-055. [Online]. Available: https://www.emerald.com/insight/content/doi/10.1108/AA-06-2013-055/full/html

[3] ACTUATECH, "Production process – pneumatic actuators made in actuatech," 2021, https://www.actuatech.com/company/production-process.html (Juli 2021).

[4] R. Liu, Z. Wang, T. Sparks, F. Liou, and J. Newkirk, "Aerospace applications of laser additive manufacturing." Elsevier, 2017, pp. 351–371. [Online]. Available: https://www.sciencedirect.com/science/article/pii/B9780081004333000130

[5] C. Culmone, G. Smit, and P. Breedveld, "Additive manufacturing of medical instruments: A state-of-the-art review," *Additive Manufacturing*, vol. 27, pp. 461–473, 2019. DOI: 10.1016/j.addma.2019.03.015. [Online]. Available: https://www.sciencedirect.com/science/article/abs/pii/S2214860418308911

[6] K. Batkuldinova, A. Abilgaziyev, E. Shehab, and M. Ali, "The recent development of 3D printing in developing lower-leg exoskeleton: A review," *Materials Today: Proceedings*, vol. 42, 02 2021. DOI: 10.1016/j.matpr.2020.12.191. [Online]. Available: https://www.sciencedirect.com/science/article/pii/S221478532039876X

[7] Z. Wang, M. Zhu, S. Kawamura, and S. Hirai, "Fabrication and performance comparison of different soft pneumatic actuators for lunch box packaging," in *2017 IEEE International Conference on Real-time Computing and Robotics (RCAR)*. IEEE, 2017. DOI: 10.1109/RCAR.2017.8311830 pp. 22–27. [Online]. Available: https://ieeexplore.ieee.org/document/8311830

[8] M. Temirel, B. Yenilmez, S. Knowlton, J. Walker, A. Joshi, and S. Tasoglu, "Three-dimensional-printed carnivorous plant with snap trap," *3D Printing and Additive Manufacturing*, vol. 3, no. 4, pp. 244–251, 2016. DOI: 10.1089/3dp.2016.0036. [Online]. Available: https://www.liebertpub.com/doi/10.1089/3dp.2016.0036

[9] K. H. Heung, Z. Q. Tang, L. Ho, M. Tung, Z. Li, and R. K. Tong, "Design of a 3D printed soft robotic hand for stroke rehabilitation and daily activities assistance," in *2019 IEEE 16th International Conference on Rehabilitation Robotics (ICORR)*. IEEE, 2019. DOI: 10.1109/ICORR.2019.8779449 pp. 65–70. [Online]. Available: https://ieeexplore.ieee.org/document/8779449

[10] J. Krause and P. Bhounsule, "A 3D printed linear pneumatic actuator for position, force and impedance control," in *Actuators*, vol. 7, no. 2. Multidisciplinary Digital Publishing Institute, 2018. DOI: 10.3390/act7020024 p. 24. [Online]. Available: https://www.mdpi.com/2076-0825/7/2/24

[11] C. L. Nall and P. A. Bhounsule, "A Miniature 3D Printed On-Off Linear Pneumatic Actuator and Its Demonstration into a Cartoon Character of a Hopping Lamp," in *Actuators*, vol. 8, no. 4. Multidisciplinary Digital Publishing Institute, 2019. DOI: 10.3390/act8040072 p. 72. [Online]. Available: https://www.mdpi.com/2076-0825/8/4/72

[12] I. Martinez de Apellaniz Goenaga, "Development of a 3D printed hydraulic piston-cylinder system," Master's thesis, Delft University of Technology, 2019. [Online]. Available: http://resolver.tudelft.nl/uuid:e5792702-442e-419a-a8b5-c28394fe0904
[13] V. Groenhuis and S. Stramigioli, "Laser-cutting pneumatics," *IEEE/ASME transactions on mechatronics*, vol. 21, no. 3, pp. 1604–1611, 2015. DOI: 10.1109/TMECH.2015.2508100. [Online]. Available: https://ieeexplore.ieee.org/document/7353189
[14] X. Tran and H. Yanada, "Dynamic Friction Behaviors of Pneumatic Cylinders," *Intelligent Control and Automation*, vol. 04, pp. 180–190, 01 2013. DOI: 10.4236/ica.2013.42022. [Online]. Available: https://www.scirp.org/journal/paperinformation.aspx?paperid=31741
[15] P. A. O. Adegbuyi and I.-L. Marcu, "Hydraulic and pneumatic cylinder failures, the effect of fluid cleanliness on component life," *Hidraulica*, no. 1, 2013.
[16] ERIKS, "Wanneer gebruikt U een X-ring?" June 2021, https://shop.eriks.nl/nl/wanneer-wordt-gebruik-gemaakt-van-een-x-ring/ (June 2021).
[17] ERIKS, "Merkel zuigerafdichting NAP310," Tech. Rep., 08 2015.
[18] ERIKS, "Zuigerafdichting NAPN 80 NBR," Tech. Rep., 08 2015.
[19] ERIKS, "Merkel zuigerafdichting Airzet PK," Tech. Rep., 12 2015.
[20] ERIKS, "Merkel compactafdichting KDN," Tech. Rep., 08 2015.
[21] ERIKS, "O-ring technical handbook," ERIKS, Tech. Rep.
[22] Formlabs, "Clear Resin 1 L – RS-F2-GPCL-04," July 2021, https://formlabs.com/store/clear-resin/ (July 2021).
[23] G. Belforte, G. Mattiazzo, S. Mauro, and L. Tokashiki, "Measurement of Friction Force in Pneumatic Cylinders," *Tribotest*, vol. 10, pp. 33 – 48, 09 2003. DOI: 10.1002/tt.3020100104. [Online]. Available: https://onlinelibrary.wiley.com/doi/10.1002/tt.3020100104
[24] D. B. Wassink, V. G. Lenss, J. A. Levitt, and K. C. Ludema, "Physically Based Modeling of Reciprocating Lip Seal Friction," *J. Trib.*, vol. 123, no. 2, pp. 404–412, 2001. DOI: 10.1115/1.1310370. [Online]. Available: https://www.doi.org/10.1115/1.1310370
[25] G. Belforte, A. M. Bertetto, and L. Mazza, "Test rig for friction force measurements in pneumatic components and seals," *Proceedings of the Institution of Mechanical Engineers, Part J: Journal of Engineering Tribology*, vol. 227, no. 1, pp. 43–59, 2013. DOI: 10.1177/1350650112453522. [Online]. Available: https://journals.sagepub.com/doi/10.1177/1350650112453522
[26] Sensortechnics, "CTE8000 / CTU8000 Series - OEM pressure transmitters for industrial media," Tech. Rep., http://www.farnell.com/datasheets/1581372.pdf (June 2021).
[27] M. Siegfarth, T. P. Pusch, A. Pfeil, P. Renaud, and J. Stallkamp, "Multi-material 3D printed hydraulic actuator for medical robots," *Rapid Prototyping Journal*, 2020. DOI: 10.1108/RPJ-07-2019-0205. [Online]. Available: https://www.emerald.com/insight/content/doi/10.1108/RPJ-07-2019-0205/full/html

The cover of this thesis has been designed using resources from Freepik.com (https://www.freepik.com/) and from 123RF (https://nl.123rf.com/).

APPENDIX A
LEAKAGE AND POSSIBLE BREAKDOWN OF 3D-PRINTED AIR CHAMBERS

A. Introduction

We started this research by analysing the possibility of creating non-porous, and thus leakage-free 3D-printed air chambers. To ensure that the actuators in this research do not have porous material properties, in this preliminary research we decided which printing method was used in the rest of this study. Within this research two AM methods will be taken into account. The first method is fused deposition modelling (FDM). With this method a moving heated nozzle melts a thin layer of thermoplastic material. Layer-by-layer a three-dimensional object is created. The print layers are clearly visible on the surface of a FDM print. Worldwide this is the most widely used technique and nowadays is even available to hobbyists as a result of the low price. The most widely used material which can be printed with this method is polylactic acid (PLA). The second method which is tested is stereolithography (SLA). SLA printing, also called resin printing, was the first 3D-printing technique to be commercialised [2]. It uses a photochemical process to form the layers. Light causes chemical monomers to form polymers in the form of the desired three-dimensional shape. An ultraviolet laser is focused on a reservoir of liquid photopolymer resin. The UV laser is used to draw a pre–programmed design on the surface of the photopolymer reservoir. The resin solidifies and forms a single layer of the desired object. The completed part is then washed with a solvent to clean wet resin from the surface. Supports are needed and are to be removed manually. Naturally, the following question arises: *what 3D-printing methods can be considered to approach a leakage-free 3D-printed compressed-air chamber?*

B. Methodology

1) Printing settings: Several different printing settings were evaluated and tested on the air-tightness. Beside 3D-printed models, an aluminium model was manually created. The assumption is that this model can be seen as non-porous and can thus act as a baseline for this test. Table VI gives an overview of the different tests performed.

2) Design of the air chamber: For the purpose of this preliminary study, a hollow object was designed which can be printed without support with a FDM printer. The choice for designing the air chamber for FDM printing, as opposed to SLA printing, was made because the supports of FDM printing are created in a structure which could retain the air inside. SLA supports have the shape of 'pillars' where air can easily flow past. Therefore the air chamber is designed with a maximum printing angle of $45\,\mathrm{deg}$. A technical drawing of this design can be found in Appendix F.

3) Experimental setup: Figure 21 gives a schematic overview of the test setup. The test setup consists of the 3D-printed compressed-air chamber to be tested, connected to a pressure sensor (SensorTechnics CTU8000) and an air inlet. The air chamber is pressurised with compressed air and the air inlet is controlled with a manual control valve (Festo Shut-off valve). Prior to testing, the models are prepared with the following steps.

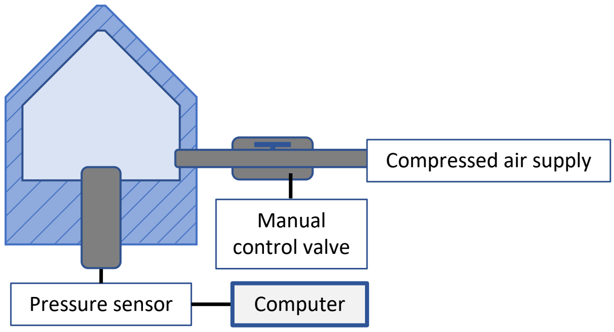

Fig. 21: Schematic overview of the test of 3D-printed compressed-air chambers

1) After washing and curing the 3D-printed models, the supports are removed manually.
2) The models are tapped with a M5 tap for the air inlet and a G1/8 tap for the pressure sensor.
3) The air inlet and pressure sensor are installed in the air chamber using Teflon tape to increase the sealing.

The test consist of the following steps:

1) When necessary an offset value is applied to the pressure sensor ensuring a starting pressure of $0\,\mathrm{MPa}$.
2) The 3D-printed air chamber is pressurised to $1\,\mathrm{MPa}$ ($10\,\mathrm{bar}$) gauge pressure, or the maximum pressure provided by the compressor.
3) The manual valve is closed to create a closed system.
4) The compressed air is disconnected to ensure that no air can enter the system.
5) The compressed air is measured for 120 seconds and transferred to the computer via LabVIEW.

A drop in pressure can be interpreted as the leakage. To make sure that the air escaping is only leakage through the 3D-printed material, the test is performed in a bucket of water. This visualises the air escaping by the bubbles forming under water making sure no air escapes at the pneumatic connectors.

4) Repeatability of the test results: In order to find the variation within our measurements, a repeatability test was performed on one of the models. This consisted of two steps. Firstly, we ran the measurements for three times in a row, without changing the connections of the air inlet and pressure sensor. Secondly, the air inlet and pressure sensor were disconnected and reconnected prior to taking the test. Again, the test was performed three times, while reconnecting the model every time, to find the variation within our results.

C. Results

Pictures of the test setup to measure the leakage through the material of the 3D-printed air chamber can be seen in Figure 22 and Figure 23. The maximum pressure that was reached during this test was approximately $0.75\,\mathrm{MPa}$, which was the maximum pressure reached by the used compressor.

TABLE VI: Different printing aspects tested for breakdown and leakage

Production method	Printer	Material	Layer thickness	Infill %
Machining	-	Aluminium	-	-
FDM	Ultimaker 3 extended	PLA black	0.2 mm	100
FDM	Ultimaker 3 extended	PLA black	0.15 mm	100
FDM	Ultimaker 3 extended	PLA black	0.1 mm	100
FDM	Ultimaker 3 extended	PLA black	0.06 mm	100
SLA	Prusa SL1	Prusa Grey Tough	0.05 mm	-
SLA	Formlabs 3	Clear resin V4	0.1 mm	-

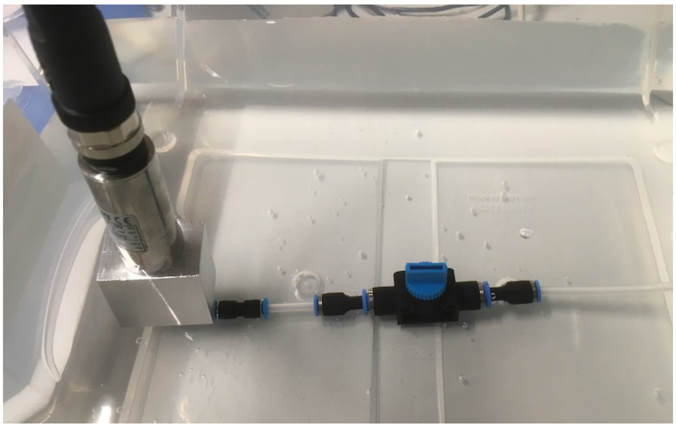

Fig. 22: The aluminium model during the test

Fig. 23: The SLA model prior to the test

Therefore, it was not possible to test the entire range of pressure in which pneumatic actuator might work — this is usually up to 1 MPa. The pressure drop in the 3D-printed air chambers can be seen in Figure 24. There is a wide deviation in leakage between the different models. Five of the seven chosen models were able to keep the pressure inside the compressed-air chamber for the two minutes of this test. Two of the models, the FDM printed models with layer height of 0.15 mm and 0.20 mm, could not hold the 0.75 MPa of pressure which was put on these models. To distinguish between the remaining models, the results in Figure 24(b) can be observed. When looking at the FDM-printed models, we can observe that the model with the smallest layer height (0.06 mm) has the smallest pressure-loss. The best performing models are the aluminium model and the SLA model which is printed with the Formlabs printer. These models lose about 0.003 MPa over the test, which is only 0.04 % of its starting pressure.

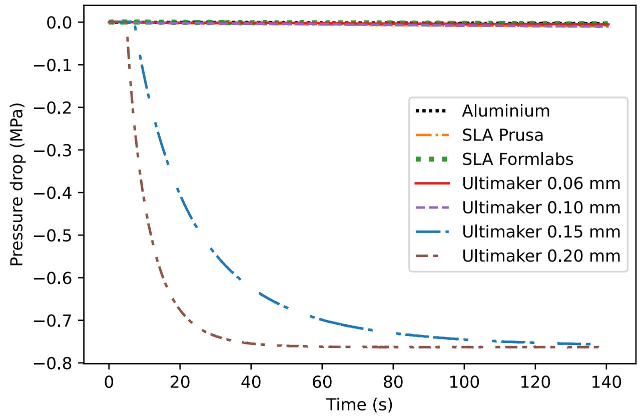

(a)

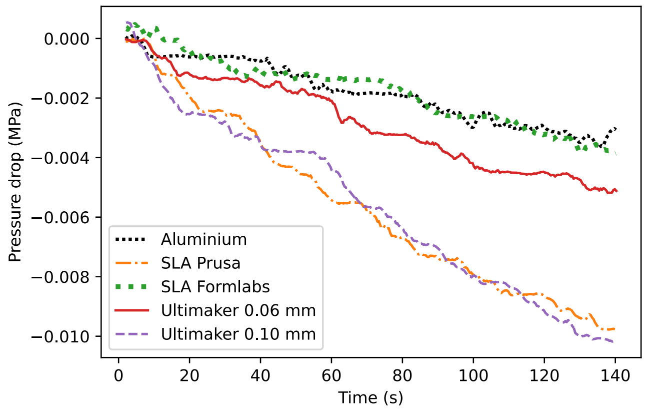

(b)

Fig. 24: Leakage in the 3D-printed compressed-air chambers. Seven models were compared; four FDM printed models, two SLA printed models and an aluminium version which acted as a baseline (a). In Figure (b), the FDM model of 0.15 mm and 0.20 mm layer thickness were removed for better comparison.

1) Repeatability: For the repeatability test, two different models were used. The repeatability test where the test was merely rerun, was taken with the SLA Formlabs model of which the results can be found in Figure 25(a). We wanted to use this same model for the reconnecting-repeatability test. However, due to damages at the thread of the pneumatic connectors, it was not possible to reconnect this model three times. Therefore the test where the model was reconnected was performed with the Ultimaker $0.06\,\mathrm{mm}$ layer height model.

D. Discussion

1) Connecting points: The results show us that all the models have a slight pressure loss, even the aluminium version. We think that a small amount of air escaped the air chamber at the place where it is connected to the pressure sensor and the air-inlet. This was not enough to form visible bubbles, but due to the relatively low total volume of the air chamber, this pressure drop can be observed in the data. We can also observe this when looking at the repeatability test. Comparing the two tests shows us that reconnecting the model gives some variation in the data (Figure 25(b)), which could not be observed when merely rerunning the test (Figure 25(a)).

2) FDM printing: Two of the models could not hold the pressure in the tank for these two minutes: the two FDM printed models with the largest layer height – $0.20\,\mathrm{mm}$ and $0.15\,\mathrm{mm}$. These models were also the only two models where air bubbles were visible on the 3D-printed material during the test. These porous models were removed in Figure 24(b) in order to compare the other models. If we compare all the FDM printed models, we can see that the models with a smaller layer height show less leakage compared to the models with a larger layer height.

3) SLA printing: We can also observe some variation between the two SLA printed models, where the model printed by the Formlabs printer performed better than the model printed on the Prusa printer. Although we varied both the printer and the material between these models, we think that the difference between these models can be explained by a different material brittleness and therefore the ease of connecting the models.

E. Conclusion

In this preliminary study we hypothesised on the possibility to create a leakage-free 3D-printed compressed-air tank. We showed that printing a leakage-free compressed-air chamber with SLA is possible, tested up to a pressure of $0.75\,\mathrm{MPa}$. While printing with FDM, the layer height proved an important factor — a higher-precision FDM printed air-tank with a layer height of $0.06\,\mathrm{mm}$ can be considered leakage-free at the tested pressure of $0.75\,\mathrm{MPa}$.

Appendix B
The installation guides for the sealing mechanisms

This appendix contains information about the installation of the different sealing mechanisms. The dimensions of an O-ring are given in inner diameter (ID) and cross-section, also called section (S). The sealings used in this study were chosen for an outer diameter (OD)

$$OD = ID + 2 \cdot S \tag{4}$$

TABLE VII: Dimensions of the sealing mechanisms

Sealing mechanism	ID	S	OD
ERIKS O-ring	$18.64\,\mathrm{mm}$	$3.53\,\mathrm{mm}$	$25.7\,\mathrm{mm}$
ERIKS X-ring	$18.64\,\mathrm{mm}$	$3.53\,\mathrm{mm}$	$25.7\,\mathrm{mm}$
Parkside O-ring	$18\,\mathrm{mm}$	$3.5\,\mathrm{mm}$	$25\,\mathrm{mm}$
Sealing mechanism	ID / d_N	W_{PG} / L	OD / D_N
KDN	$17.9\,\mathrm{mm}$	$2.1\,\mathrm{mm}$	$25\,\mathrm{mm}$
PK	$18\,\mathrm{mm}$	$2.5\,\mathrm{mm}$	$25\,\mathrm{mm}$
NAP310	$19\,\mathrm{mm}$	$3.5\,\mathrm{mm}$	$25\,\mathrm{mm}$
NAPN	$17\,\mathrm{mm}$	$5.5\,\mathrm{mm}$	$25\,\mathrm{mm}$

of $25\,\mathrm{mm}$. Due to limited availability the X-ring was chosen as the closest available option with an OD of $25.7\,\mathrm{mm}$. For the X-ring and the O-ring the gland was designed for a specific squeeze ratio, r_{sq}. In this study a squeeze ratio of 0.1 (10%) was used, which is within the range recommended by the manufacturer [21].

$$S_{sq} = S \cdot (1 - r_{sq}) \tag{5}$$

The squeezed dimension of the O-ring (S_{sq}) was used to calculate the piston groove diameter (D_{PG}).

$$D_{PG} = OD - 2 \cdot S_{sq} \tag{6}$$

Figure 26 gives a visual illustration of the key dimensions of the seal gland. The width of the piston groove W_{PG} is chosen as $1.0\,\mathrm{mm}$ more than the cross-section based on professional opinion of the lab technicians. The clearance (C) between the piston and cylinder was set on $0.5\,\mathrm{mm}$. For the other sealing mechanisms, the guides produced by the manufacturer were used for the dimensions of the sealing grooves. The sealing mechanisms were selected for a cylinder bore size of $25\,\mathrm{mm}$. The measurements of the sealing mechanisms are given with an inner diameter d_N (ID), and measurement for the width of the sealing L and an outer diameter D_N (OD). The dimensions of the chosen sealings can be found in Table VII. Figure 27 shows the corresponding sealing installation guides of the manufacturer.

Appendix C
Determining the actuator dimensions

A. Stadium-shaped cylinder

The first cross-sectional shape is a shape which is closely related to a cylinder — a stadium shape. The cross-section of this shape can be seen in Figure 2(b) in Section II. In order to have a fair comparison between this model and the circular piston-cylinder systems, the shape is designed to have an equal surface area to the other tested cylinders. The surface area for the circular actuator (A_c)

$$A_c = \pi \left(\frac{d}{2}\right)^2 \tag{7}$$

is determined by the diameter (d) of the cylinder. For comparison of the models the $25\,\mathrm{mm}$ cylinder is chosen. The dimensions of the stadium model are determined by the following two equations,

$$A_s = \pi \left(\frac{D}{2}\right)^2 + DL \tag{8}$$

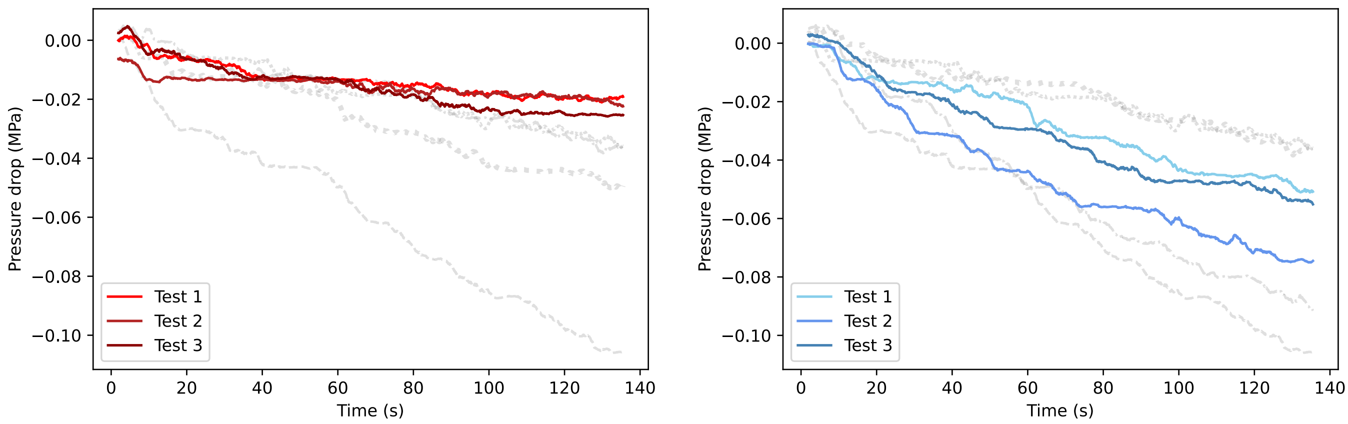

(a)

(b)

Fig. 25: The repeatability results of leakage in compressed-air chambers where (a) the test was rerun without any changes in the connections and (b) the model was reconnected prior to taking the tests.

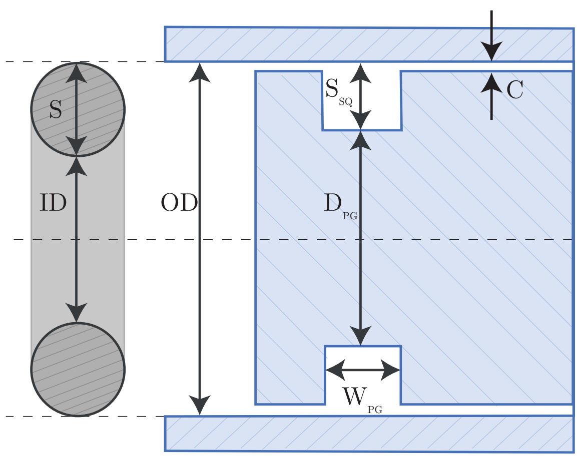

Fig. 26: The key dimensions of the sealing and piston groove

$$P_s = \pi D + 2L \tag{9}$$

where A_s is the cross-sectional surface area and P_s is the perimeter of the stadium-shaped pneumatic actuator. A slightly larger O-ring was used for this model, with an inside diameter of $22\,\text{mm}$ with a cross-sectional thickness of $3.5\,\text{mm}$). With these equations the values for L and D are determined.

B. Kidney-shaped cylinder

The second actuator which we tested has the shape of a kidney, a cross-section of which can be seen in Figure 2(c). This shape has the possible advantage of being able to fit around another object. Again, we have two equations to determine the dimensions of this object. The formula for the cross-sectional area of the kidney shape (A_k) gives

$$A_k = \pi \left(\frac{a}{2}\right)^2 + \gamma \left(ra + \frac{a^2}{2}\right) \tag{10}$$

when simplified. The perimeter of the kidney shape, P_k, is calculated with

$$P_k = \pi a + \gamma(2r + a). \tag{11}$$

However, for this shape we have three unknown values. We decided to set γ on $\frac{5}{9}\pi$, which is the equivalent of $100°$ – a slightly obtuse angle, with the ability to fit around an object.

Appendix D
The first iteration of the test setup

A. Introduction

In this section we describe the first iteration of the test setup and the steps taken to validate the setup.

1) Dynamic leakage - expected results: During the dynamic leakage test the piston moves inside the cylinder, while a closed system is created. Therefore we would expect the measured pressure value at a fixed position to slightly drop during the tests if leakage is present. If no leakage is present the pressure at this point will remain constant.

2) Friction force - expected results: During the test to determine the friction force, the piston is moved back and forth inside the cylinder. Because the friction force always acts in the opposite direction of the velocity of the piston, see Figure 28, we expect the measured friction force to deviate between a negative value for the extending stroke, and a positive value for the retracting stroke.

B. Method

1) Initial test setup: A first iteration of the test setup is shown in Figure 29. The electrical cylinder (A) with its power source (B), is positioned on a wooden plate. The laser sensor (C) is placed at the end of the electrical actuator. The data of the laser sensor is used to control the actuator. At the end of the moving piston of the electrical actuator, the force sensor is placed (D). The last sensor in the test rig is the Pressure

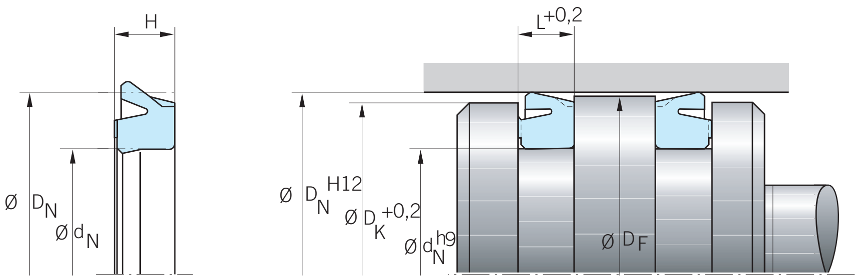

(a) NAP310 single-acting sealing [17]

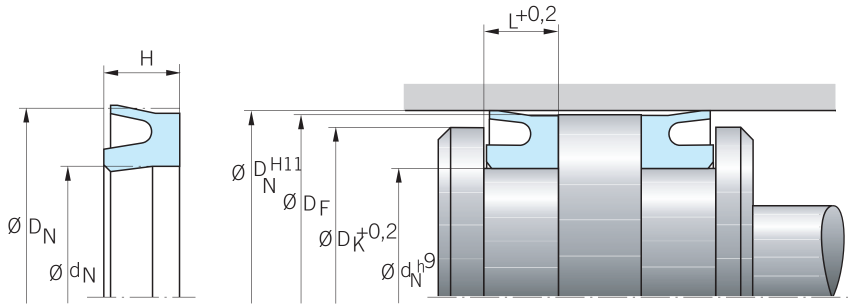

(b) NAPN single-acting sealing [18]

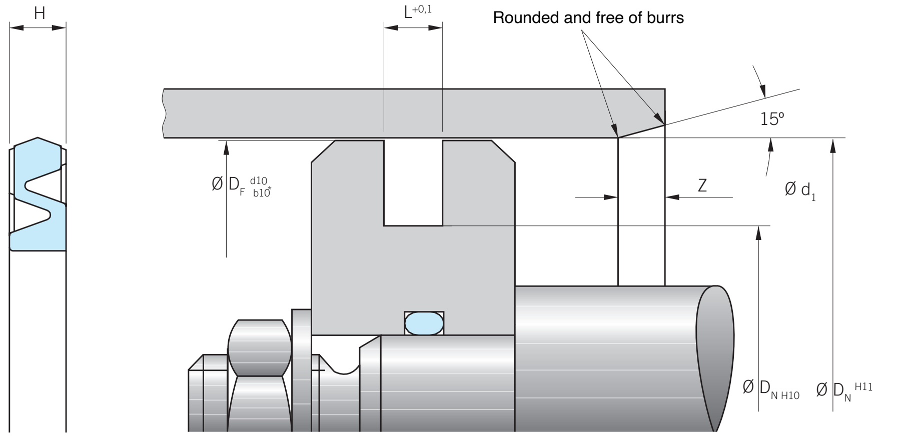

(c) PK double-acting sealing [19]

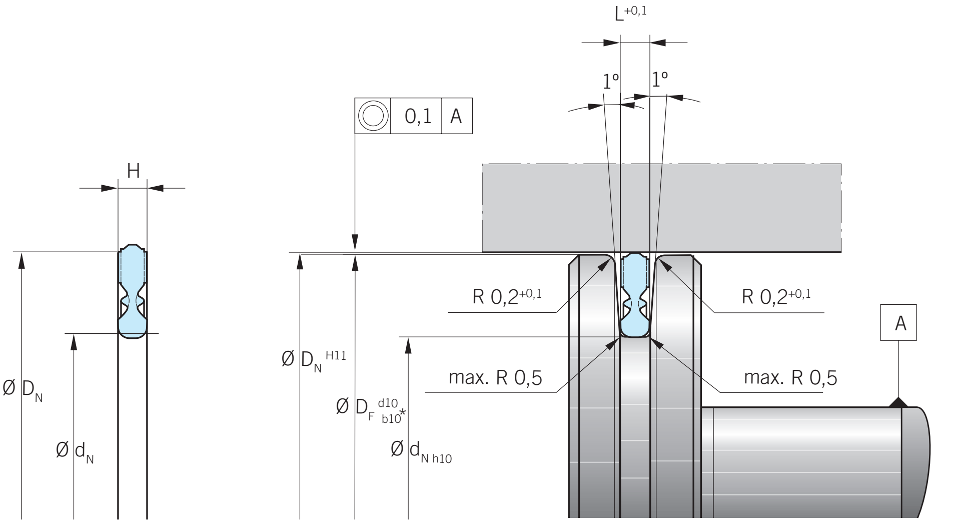

(d) KDN double-acting sealing [20]

Fig. 27: Guidelines for groove dimensions for the sealing mechanisms

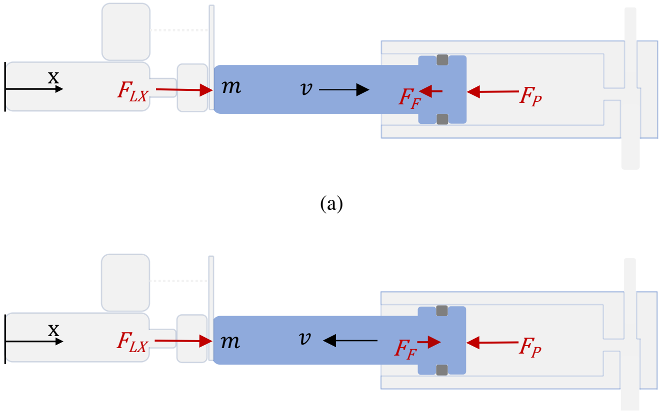

(a)

(b)

Fig. 28: FBD for the extending(a) and retracting stroke(b)

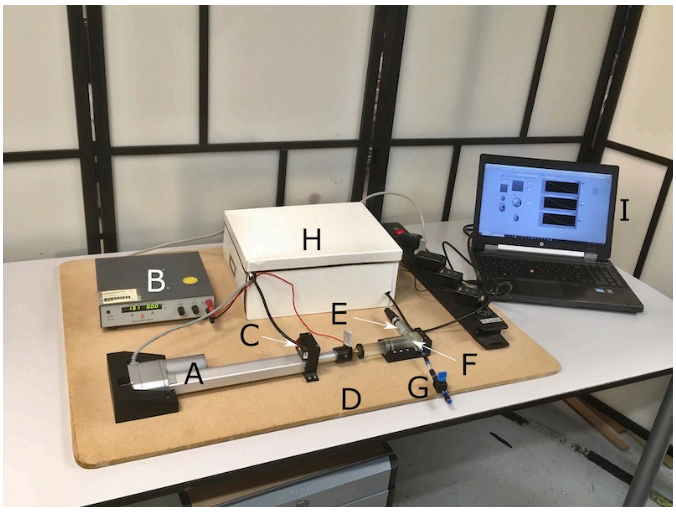

Fig. 29: A picture of the initial test setup consisting of an electrical cylinder (A) with its power source (B), a laser sensor (C), a force sensor (D), a pressure sensor (E), the test model (F), a pressure inlet with manual control valve (G), a box with electronical components (H) connecting the sensors via LabVIEW to a computer (I).

sensor (E), which is connected to the 3D-printed tested piston-cylinder system (F). On the other side of the test model, an air inlet is connected via a manual control valve (G). The data is gathered via an electrical circuit (H) and transferred via LabVIEW to the computer (I). Two tests were performed to validate the test rig and find irregularities.

2) Initial dynamic leakage test: The first test performed was the dynamic leakage test. To validate the results of this test, the test was performed with the same model for several different aspects which might influence the results.

- We checked if the pressure sensor provides a value of $0\,\mathrm{MPa}$ when no pressure is applied.
- We checked if moving the air tubes around during the test could have an influence on the leakage results.
- We checked the influence of proper closing the manual control valve.
- We checked the influence of the orientation of the piston in the cylinder during the test.
- We checked if the non-axial gravitational force of the piston created a deviation in the results.

3) Initial friction force test: The second test performed was the test to determine the friction force in the test model. Some validation steps were performed on the test model.

- We checked if the pressure sensor provides a value of $0\,\mathrm{MPa}$ when no pressure is applied.
- We checked if the force sensor provides a value of $0\,\mathrm{N}$ when no force is applied.
- We checked if the pressure remained constant during the tests.
- We checked if the friction force showed a logical behaviour, showing a negative value for the extending stroke and a positive value for the retracting stroke.
- We checked the influence of the orientation of the piston in the cylinder during the test.

C. Results and discussion

1) Initial dynamic leakage tests: Figure 30 shows the results of one of the performed tests. Some of the factors did show an influence on the initial results.

- The pressure sensor gives a value of almost $0\,\mathrm{MPa}$ when there is no pressure on the system. However, the sensor gives a gauge pressure as output. As the atmospheric pressure slightly changes over the course of several days, this can give a small deviation. Therefore, prior to starting every test an offset value was applied to ensure a starting pressure of $0\,\mathrm{MPa}$.
- The connecting tubes should not be moved too much during the test, because this may result in leakage at the connecting parts.
- It is important to properly close the manual control valve before starting the test. When the tap is only slightly opened, air can leak through.
- The orientation of the piston in the cylinder did not show different tests results with this validation step.
- Due to gravity of the piston, the angle of the piston slightly changed during the test. This should be counteracted to prevent leakage.
- Furthermore, during the test checks, we found out that pneumatic connectors which connect the system to the manual control valve only work properly when the air tube is cut in a neat straight line. We therefore checked all the connectors prior to the test.

2) Initial friction force tests: The raw data of the sensors is shown in Figure 31(a). We can see in this figure that during the test the pressure does alternate slightly between the set pressure level. This phenomenon can have three explanations;

- First of all, the total volume of the system slightly changes when the piston moves back and forth. To test this theory we added an extra volume to the system. However, this did not have an effect on the gathered data.
- The second factor of influence could be the maximum flow rate which can be reached due to the relatively narrow air tubes.

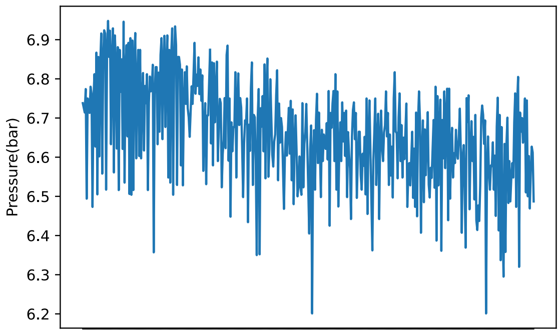

(a) Test 1

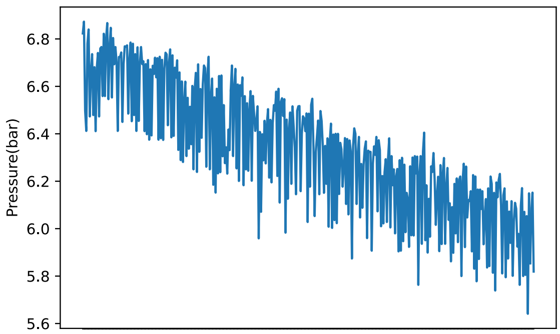

(b) Test 2

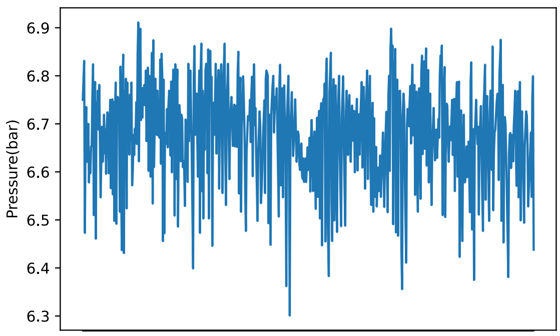

(c) Test 3

Fig. 30: The dynamic leakage test, repeated three times

- The third reason for these value is the hysteresis in the pressure sensor.

To take the pressure difference into account when calculating the frictional force, we calculated the theoretical force with the data from the pressure sensor with equation (2). The theoretical force and the measured force can be seen in Figure 31(b). The friction force was then determined by taking the difference between the theoretical force and the force measured by the force sensor, see equation (3). The friction force determined for this initial test can be seen in Figure 31(c). Remarkable when looking at this figure is that the dynamic friction force stays positive at all time. The other steps performed for the validation helped finding the results of this irregularity.

- We checked the value of the force sensor when no force was applied. This value was just above zero. In the final test an offset value was applied to ensure a starting force of 0 N.

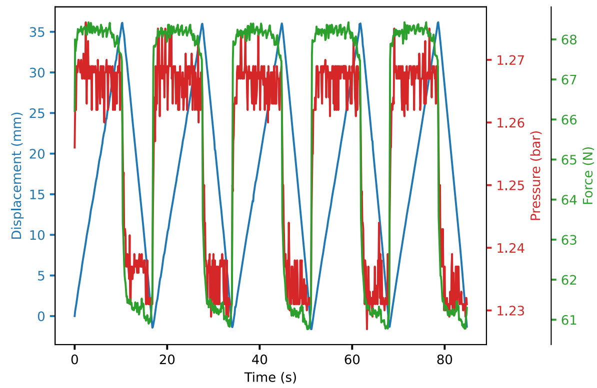

(a)

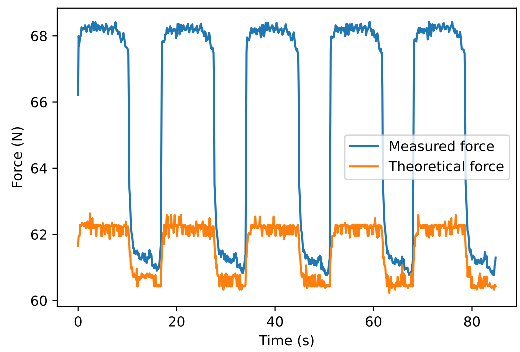

(b)

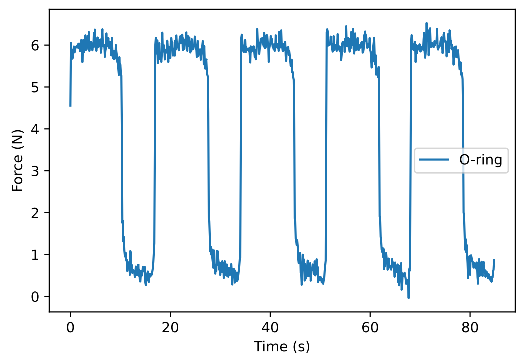

(c)

Fig. 31: (a) The raw data of the initial friction test, (b) the measured force compared to the calculated force based on the pressure input, and (c) the calculated dynamic friction force.

- We checked the scaling of the force sensor. The method to perform this check is explained in Appendix E. We hereby found that the sensor gives the right value, but that proper alignment of the force on the sensor is important to prevent measuring non-axial forces.
- The pressure sensor gives a value of almost 0 MPa when there is no pressure on the system. However, the sensor gives a gauge pressure as output. As the atmospheric pressure slightly changes over the course of several days, this can give a small deviation. Therefore, prior to starting every test an offset value was applied to ensure a starting

pressure of $0\,\mathrm{MPa}$.
- Just like the force sensor, we checked the value of the pressure sensor. We compared our sensor with another sensor, these results are presented in Appendix E. We found out that the used pressure sensor in this study gave a slightly higher value compared to the other the sensor.
- We checked our test setup for possible deflection. We discovered visible deflection in the wooden base plate and in the 3D-printed part which was designed to hold the cylinder in its position during the test.

D. Conclusion - Improvements on the test setup

Following these two tests, we implemented some improvements for the final test rig.

- Before starting the tests, the connecting elements were checked for proper sealing. All the air tubes were cut in a neat way to prevent leakage.
- An offset value was applied to the sensors prior to every test to ensure a starting pressure of $0\,\mathrm{MPa}$ and a starting force of $0\,\mathrm{N}$.
- A part was designed to hold the manual control valve and its connectors in place during the test. This made sure we could easily close the valve completely and movements of the connectors during the leakage test was prevented.
- To make sure the piston stayed aligned during the entire test, a hole was created at the end of the piston. The force sensor was equipped with a protruding part to ensure alignment of the piston during the test.
- During the testing, we discovered that during high-pressure moments up to $10\,\mathrm{MPa}$, a deflection could be seen in the connecting wooden plate. As a solution for this we could either change the thickness of the plate, or choose a material with a higher stiffness. We chose to use an aluminium frame for the final test rig.
- Another part was deflecting too much during the tests; the 3D-printed part which was connecting the test model to the test rig. The proposed solution was again to change the shape, or the material of which the model was made. In the final design we decided this part was used only for aligning the test model. An aluminium frame was added to withhold the high axial forces occurring during the tests.
- The alignment of the test model, the force sensor and the electrical cylinder is important to make sure only the axial force is measured. Using the aluminium frame as a base solves this issue.

APPENDIX E
VALIDATION OF THE SENSORS

A. Force sensor

The validation of our force sensor consisted of two tests.

1) Masses below the sensor: In the first test a known force was compared to the force measured by the sensor. The known force was provided by the gravitational force of the known masses. The masses were placed on top of each other on a hanger with a hook, which hung directly under the sensor see Figure 32. They were placed just above the ground for safety reasons. The force was measured with the force sensor and compared to the theoretical force based on the known mass. The results of this test can be found in Table VIII.

(a)

(b)

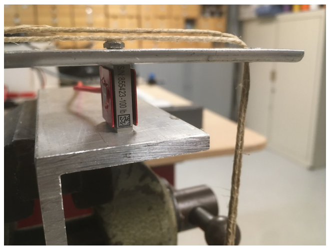

(c)

Fig. 32: The setup to validate the force sensor (a). Known masses (b) are placed below the force sensor (c).

2) Masses above the sensor: In the second test the same known masses were placed above the force sensor (see Figure 33). This second test was performed to detect the influence of moments acting on the force sensor. These moments arise when the masses are not perfectly aligned above the force sensor. The masses were added in the same order as during the previously described test, with the masses hanging below the sensor. For every extra mass the measured force was compared to the theoretical force. Table IX gives the result of this test.

TABLE VIII: The validation of the force sensor, with known masses placed below the sensor

Masses (kg)	Total mass (kg)	Theoretical force (N)	Measured force (N)	△ Force(N)
0	0	0	0	0
0,507	0,507	4,97367	5,3	0,32633
0,507 + 0,979	1,486	14,57766	14,7	0,12234
0,507 + 0,979 + 2,028	3,514	34,47234	34,6	0,12766
0,507 + 0,979 + 2,028 + 2,047	5,561	54,55341	54,7	0,14659
0,507 + 0,979 + 2,028 + 2,047 + 2,057	7,618	74,73258	74,9	0,16742
0,507 + 0,979 + 2,028 + 2,047 + 2,057 + 2.072	9,69	95,0589	95,1	0,0411
0,507 + 0,979 + 2,028 + 2,047 + 2,057 + 2.072 + 5	14,69	144,1089	144,2	0,0911
0,507 + 0,979 + 2,028 + 2,047 + 2,057 + 2.072 + 5 + 10	24,69	242,2089	242,4	0,1911
0,507 + 0,979 + 2,028 + 2,047 + 2,057 + 2.072 + 5 + 10 + 5	29,69	291,2589	291,4	0,1411

TABLE IX: The validation of the force sensor, with known masses placed on top of the sensor.

Masses (kg)	Total mass (kg)	Theoretical force (N)	Measured force (N)	△ Force(N)
0	0	0	0	0
0,439	0,429	4,20849	4,4	0,19151
0,439 + 0,979	1,408	13,81248	14,1	0,28752
0,439 + 0,979 + 2,028	3,436	33,70716	34	0,29284
0,439 + 0,979 + 2,028 + 2,047	5,483	53,78823	54,3	0,51177
0,439 + 0,979 + 2,028 + 2,047 + 2,057	7,54	73,9674	74,8	0,8326
0,439 + 0,979 + 2,028 + 2,047 + 2,057 + 2.072	9,612	94,29372	95,4	1,10628
0,439 + 0,979 + 2,028 + 2,047 + 2,057 + 2.072 + 5	14,612	143,34372	145,5	2,15628

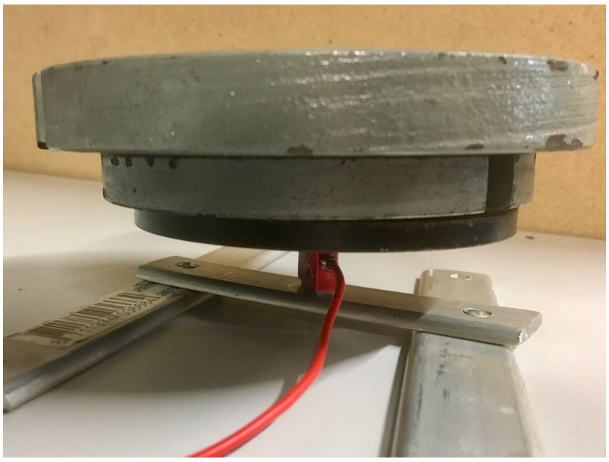

Fig. 33: The validation of the force sensor. Known masses are placed above the sensor

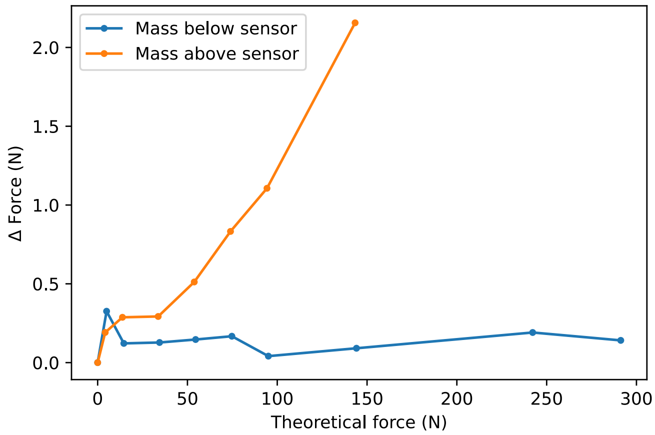

Fig. 34: Validation of the force sensor

B. Difference between the two tests

The tests were compared to find the influence of moments acting on the force sensor on the accurate measurements of axial forces. A visualisation of the results of both these tests can be found in Figure 34. These results show us that if the force is not perfectly aligned with the force sensor an error in the measurement can occur. Within this test the error was about 1.5% when the masses were placed above the sensor. These results show us that if the force sensor is not perfectly aligned with the piston-cylinder system, an error can occur in our measurements.

C. Pressure sensor

As a validation for our pressure sensor, we connected our sensor to another available sensor and measured the pressure at different pressure points with two sensors simultaneously.

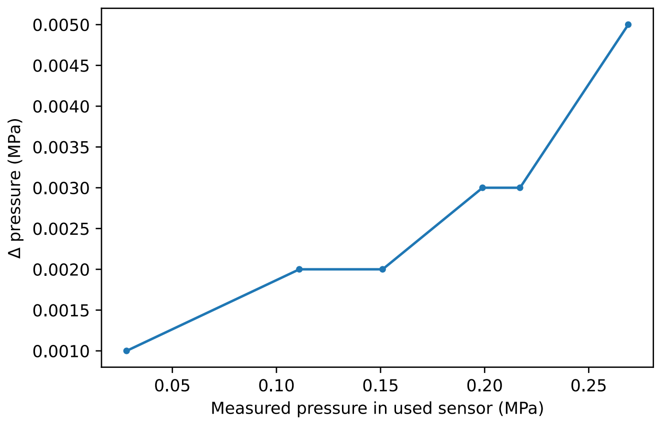

Fig. 35: Validation of the pressure sensor

TABLE X: Pressure sensor validation

Pressure sensor value (MPa)	Compared pressure sensor value (MPa)	Δp (MPa)
0.028	0.029	-0.001
0.111	0.113	-0.002
0.151	0.153	-0.002
0.199	0.202	-0.003
0.217	0.220	-0.003
0.269	0.274	-0.005

Before taking the measurements we waited for the two sensors to stabilise on the set value. The pressure sensor which was used for comparison was calibrated up to $0.25\,\mathrm{MPa}$ $(2.5\,\mathrm{bar})$. The results of this comparison can be seen in Table X and visualised in Figure 35. At $0.25\,\mathrm{MPa}$ the pressure of the sensor used in this study was about 2% lower than the sensor used for comparison.

Appendix F
Technical Drawings

The technical drawings of the tested models can be found on the final pages.

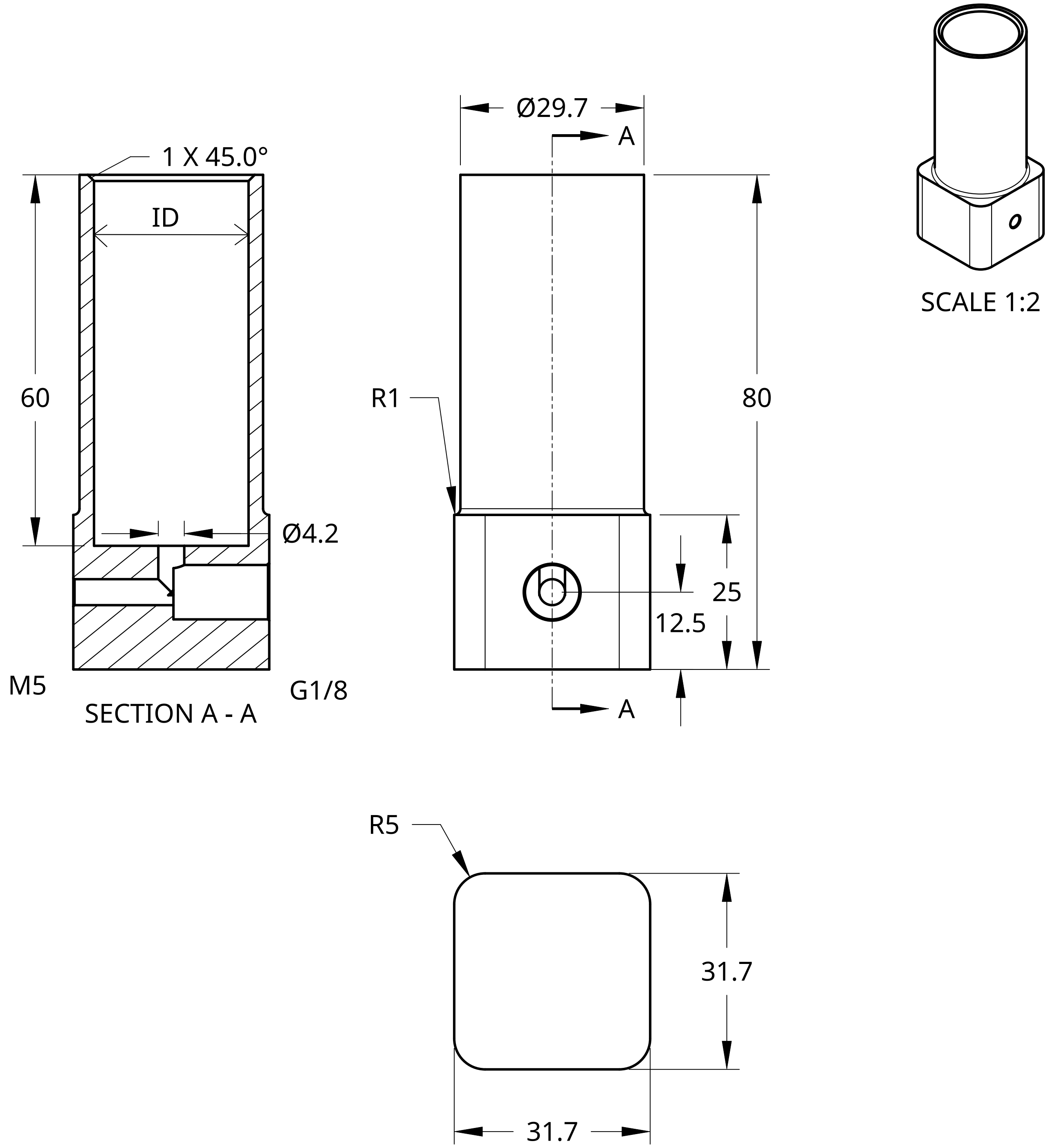

Tested model	Variable ID
Cylinder ∅25mm	25.0 mm
Cylinder ∅25.7 mm	25.7 mm

UNLESS OTHERWISE SPECIFIED, DIMENSIONS ARE IN MILLIMETERS ANGULAR = ± ° SURFACE FINISH		NAME	DATE	
	DRAWN	EVA ZILLEN	07/08/2021	TITLE
DO NOT SCALE DRAWING				Cylinder - Circle
BREAK ALL SHARP EDGES AND REMOVE BURRS				
THIRD ANGLE PROJECTION	MATERIAL Clear V4 resin	3D Printer Formlabs 3		SCALE 1:1
				SIZE A4

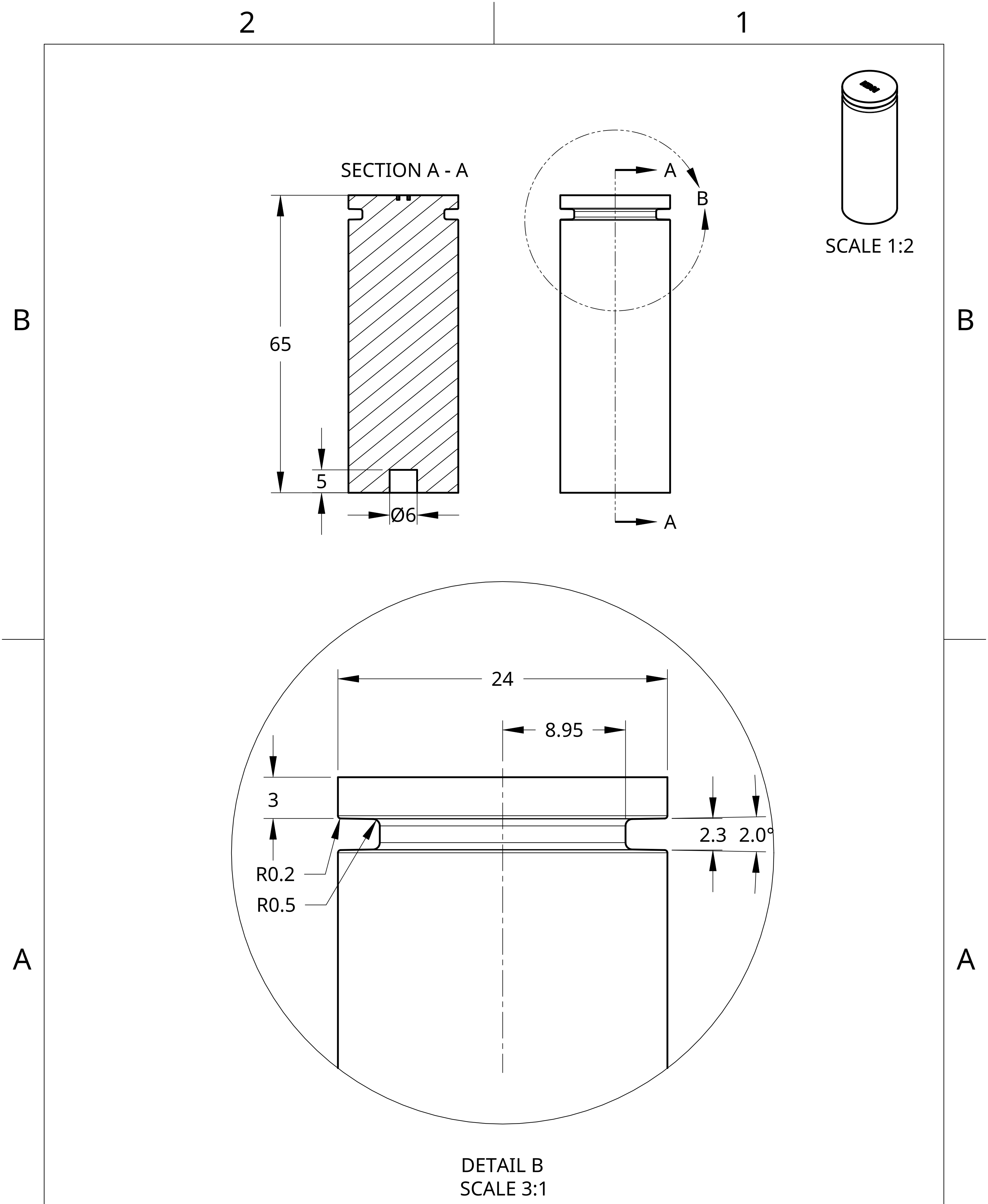

DWG NO.	SIZE	SCALE	
Piston - Circle - KDN sealing	A4	1:1	

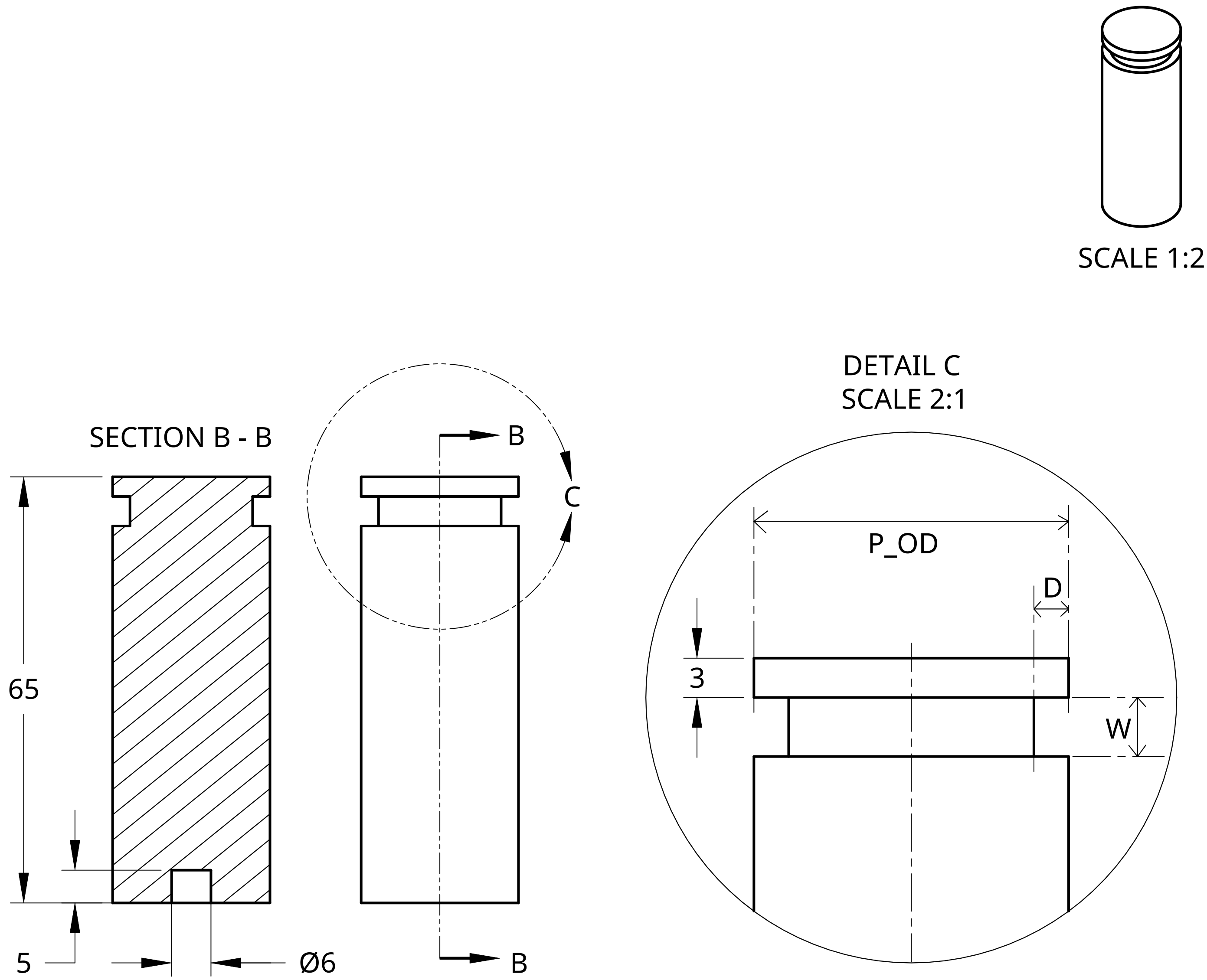

Tested model	P_OD	D	W
O-ring Ø 25mm	24 mm	2.65 mm	4.5 mm
NAPN sealing	24 mm	3.5 mm	5.7 mm
NAP310 sealing	24 mm	2.5 mm	3.7 mm
PK sealing	24 mm	3.0 mm	2.6 mm
O-ring ∅ 25.7mm	24.7 mm	2.68 mm	4.53 mm
O-ring ∅ 25.7mm	24.7 mm	2.68 mm	4.53 mm

DWG NO.	SIZE	SCALE
Piston - Circle	A4	1:1

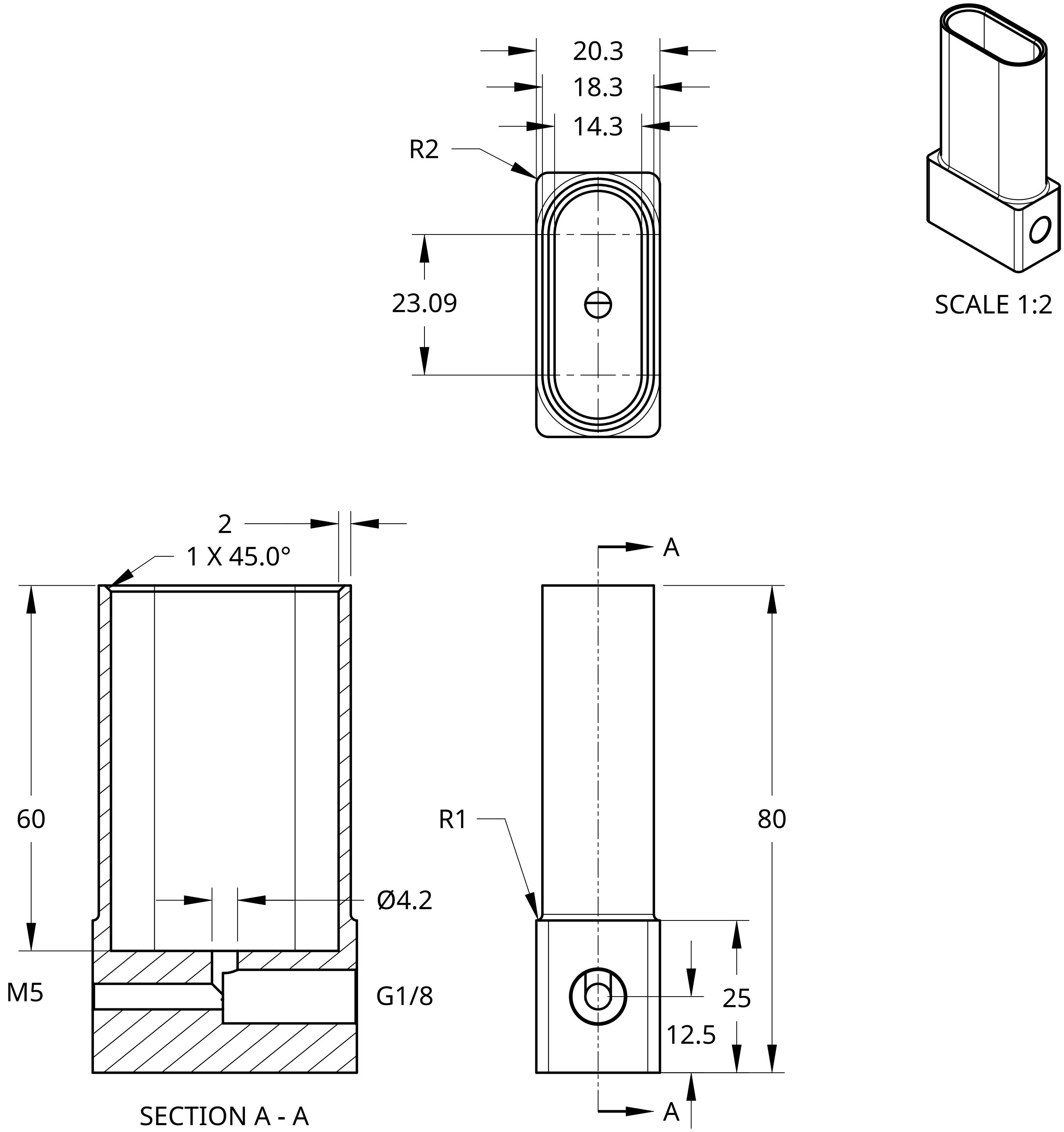

UNLESS OTHERWISE SPECIFIED, DIMENSIONS ARE IN MILLIMETERS ANGULAR = ± ° SURFACE FINISH		NAME	DATE
	DRAWN	EVA ZILLEN	07/08/2021
DO NOT SCALE DRAWING			
BREAK ALL SHARP EDGES AND REMOVE BURRS			
THIRD ANGLE PROJECTION	MATERIAL Clear V4 resin	FINISH Formlabs 3 0.1mm print layer	

TITLE

Cylinder - Stadium

SCALE 1:1

SIZE A4

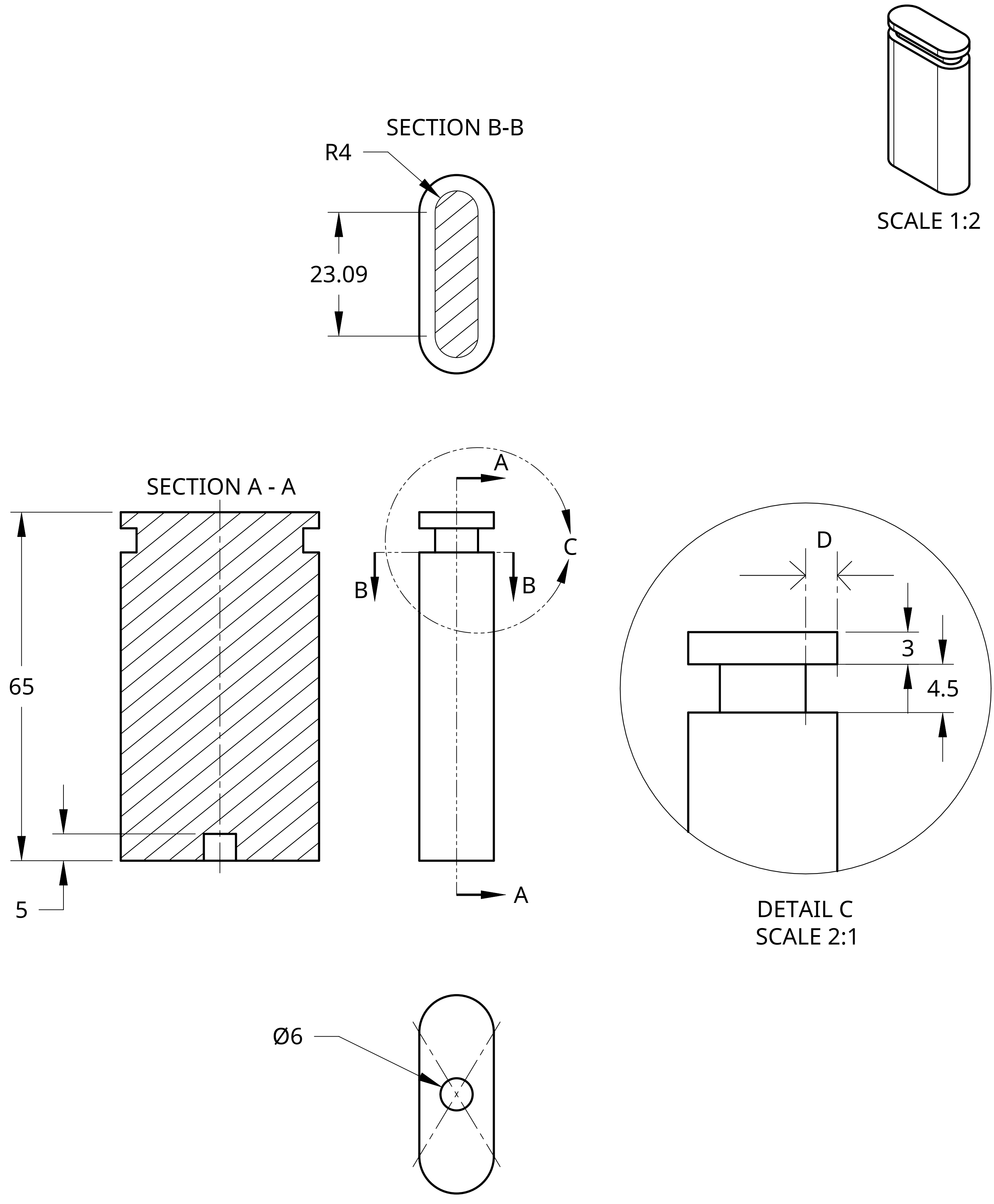

Tested model	Variable D
Clearance 0.5 mm	2.65 mm
Clearance 0.2 mm	2.95 mm

DWG NO.	SIZE	SCALE
Piston - Stadium	A4	1:1

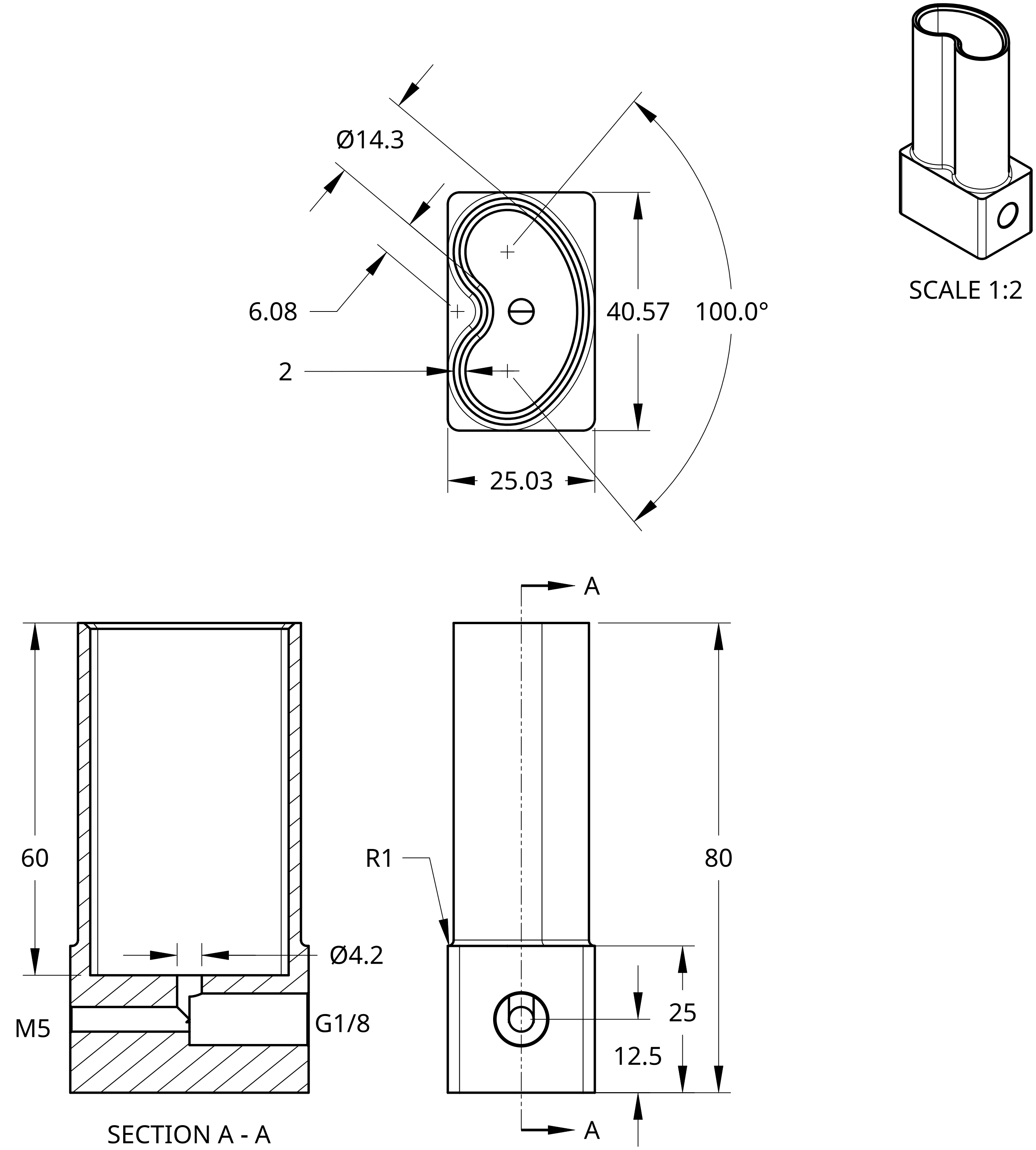

UNLESS OTHERWISE SPECIFIED, DIMENSIONS ARE IN MILLIMETERS ANGULAR = ± ° SURFACE FINISH		NAME	DATE	
	DRAWN	EVA ZILLEN	07/08/2021	TITLE Cylinder - Kidney
DO NOT SCALE DRAWING				
BREAK ALL SHARP EDGES AND REMOVE BURRS				
THIRD ANGLE PROJECTION	MATERIAL Clear V4 resin	3D printer Formlabs 3 0.1mm print layer		SCALE 1:1 SIZE A4

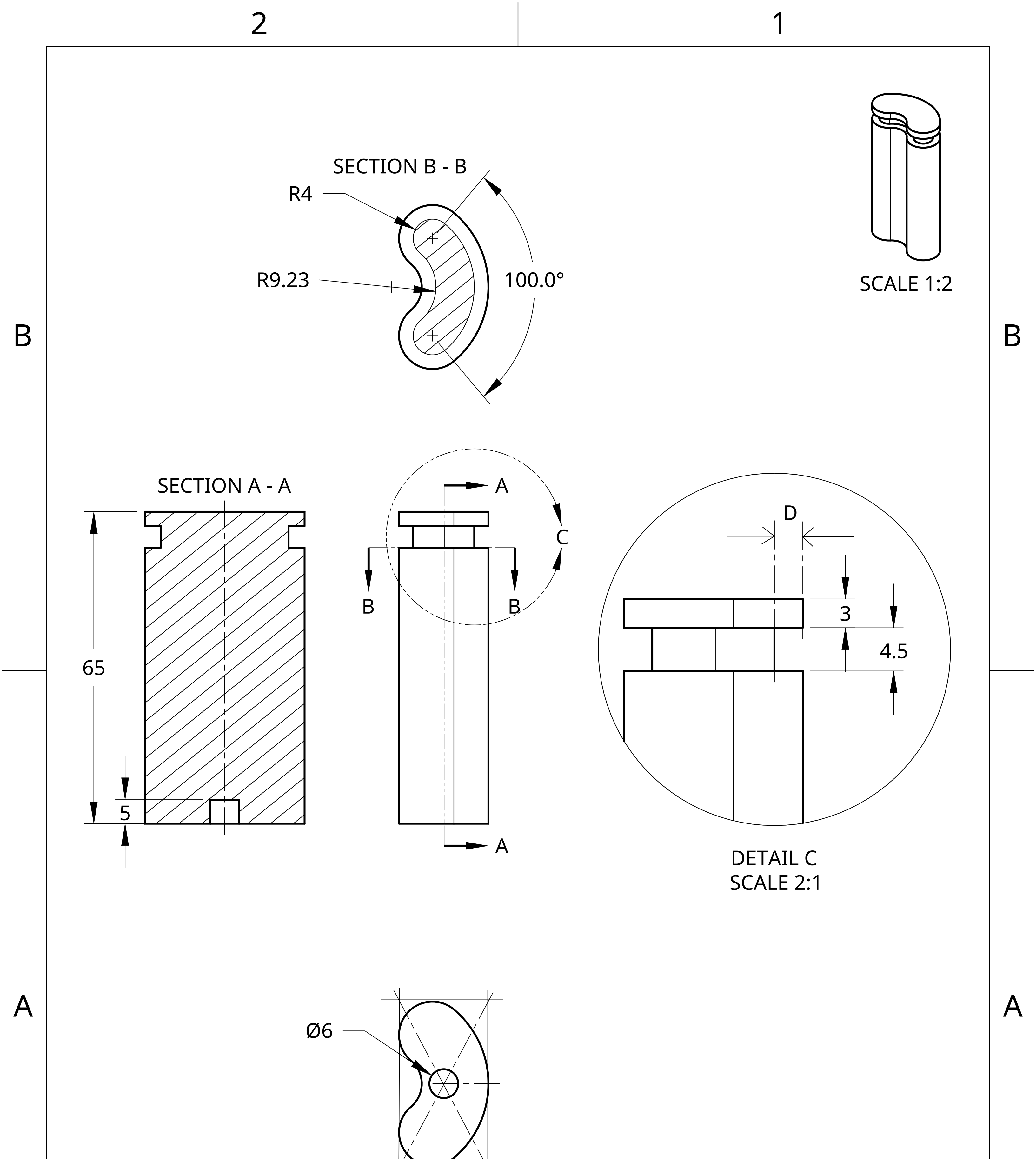

Tested model	Variable D
Clearance 0.5 mm	2.65 mm
Clearance 0.2 mm	2.95 mm

DWG NO.	SIZE	SCALE
Piston - Kidney	A4	1:1

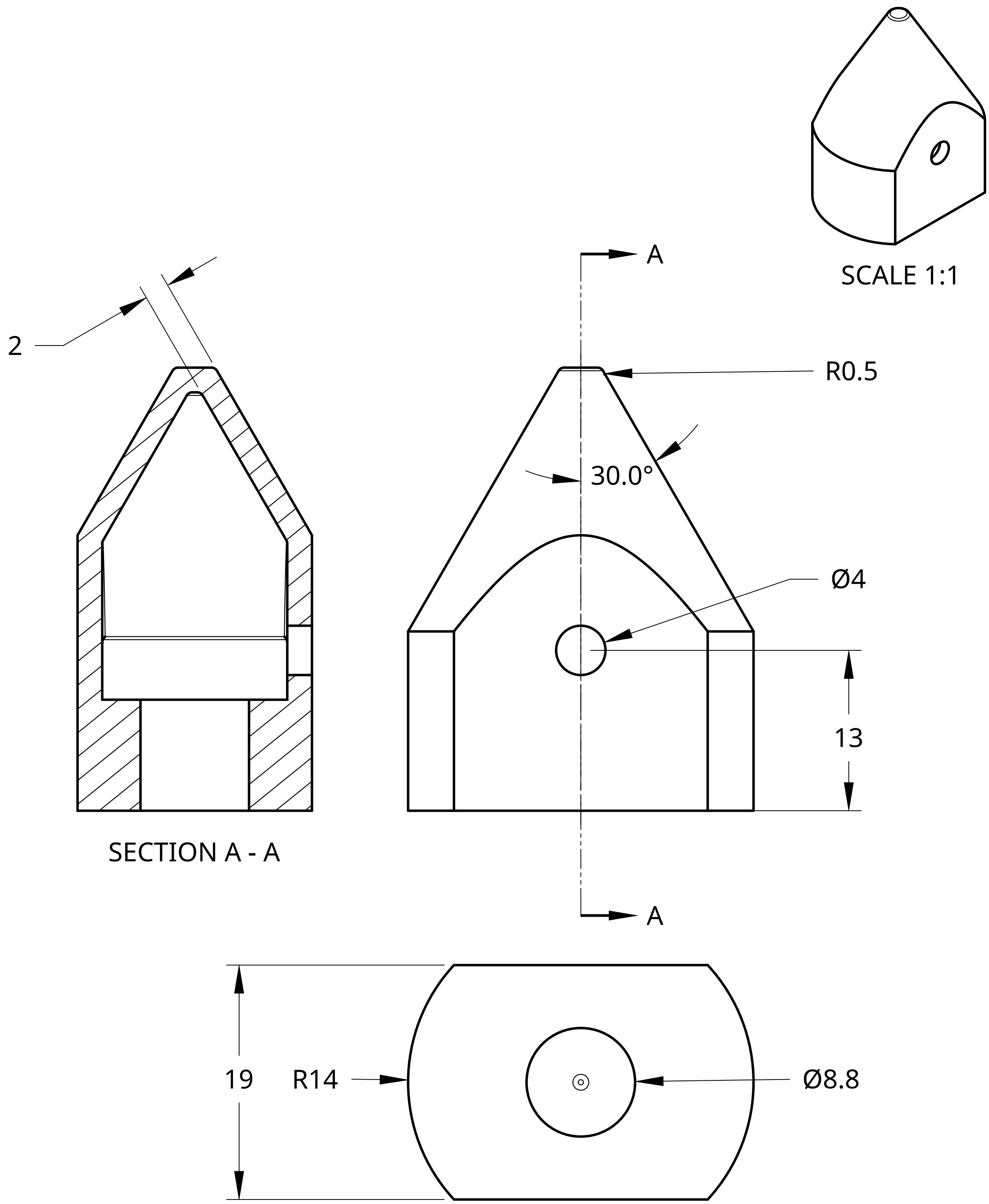

UNLESS OTHERWISE SPECIFIED, DIMENSIONS ARE IN MILLIMETERS ANGULAR = ± ° SURFACE FINISH		NAME	DATE	
	DRAWN	EVA ZILLEN	07/09/2021	TITLE Compressed-air cabin
DO NOT SCALE DRAWING				
BREAK ALL SHARP EDGES AND REMOVE BURRS				
THIRD ANGLE PROJECTION				SCALE 2:1
				SIZE A4